Nanoscale

Accepted Manuscript

This article can be cited before page numbers have been issued, to do this please use: S. Kim, J. Yeo, H. Jeong and J. Suh, *Nanoscale*, 2026, DOI: 10.1039/D5NR05242D.

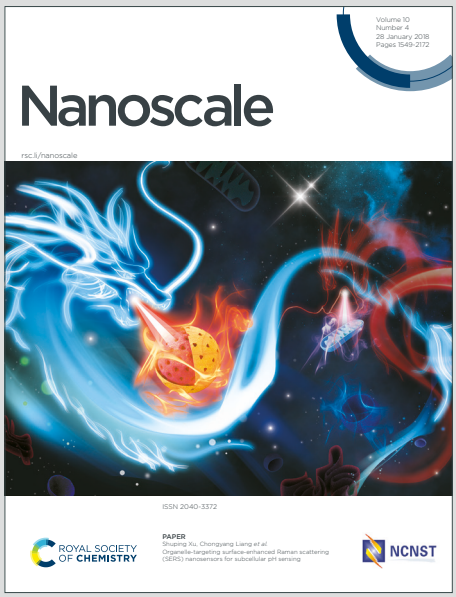

ROYAL SOCIETY OF CHEMISTRY

rsc.li/nanoscale

Counter-Doping in Two-Dimensional Transition-Metal Dichalcogenides: Flipping Native Polarity and Beyond

View Article Online
DOI: 10.1039/D5NR05242D

Sungyeon Kim[1], Jeongin Yeo[1], Hongsik Jeong[1], Joonki Suh[2,★]

[1] Department of Materials Science and Engineering, Ulsan National Institute of Science and Technology (UNIST), Ulsan 44919, Republic of Korea

[2] Department of Chemical and Biomolecular Engineering, Korea Advanced Institute of Science and Technology (KAIST), 34141 Daejeon, Republic of Korea

Correspondence and requests for materials should be addressed to J.S. (email: joonki.suh@kaist.ac.kr)

Contents

View Article Online
DOI: 10.1039/D5NR05242D

View Article Online
DOI: 10.1039/D5NR05242D

ABSTRACT

Two-dimensional (2D) transition-metal dichalcogenides (TMDs) hold immense promise for next-generation nanoelectronics and optoelectronics, yet their technological viability hinges on reliable control over carrier type and concentration. In practice, most TMDs exhibit their own characteristic native polarity set by intrinsic point defects and unintentional impurities, which fix the Fermi level and frustrate subsequent extrinsic doping approaches. That is, such native donors and acceptors not only define the as-grown electronic ground state but also complicate attempts at deliberate carrier modulation, often yielding unstable, hysteretic, or spatially non-uniform doping profiles. This mini-review first clarifies the defect-driven origins of native polarity in representative semiconducting TMDs by connecting characteristic vacancy and impurity states to experimentally observed conduction behaviors. We then survey main extrinsic doping strategies, including surface and remote charge transfer, chemical intercalation, and substitutional incorporation. While each approach presents distinct trade-offs regarding stability, controllability and device compatibility, we argue that substitutional doping, where dopant atoms replace host lattice sites, stands out as the most robust route for stable polarity control. We specifically highlight how such substitutional counter-doping, where intentional dopants override the native-defect-imposed Fermi level and flip the intrinsic carrier type, and discuss how it enables diverse device applications ranging from complementary logic and low-resistance contacts to emerging optoelectronic and neuromorphic functionalities. We conclude by outlining the key remaining issues, such as dopant activation efficiency, interfacial coupling, and wide-range carrier modulation, to guide the future developments of 2D semiconductor platforms.

View Article Online
DOI: 10.1039/D5NR05242D

1. INTRODUCTION

Two-dimensional (2D) transition metal dichalcogenides (TMDs) have rapidly evolved from scientifically intriguing quantum materials into technologically promising candidates for next-generation nanoelectronics and optoelectronics.[1-4] Their atomic thickness, clean van der Waals (vdW) interfaces, strong electrostatic gate coupling, immunity to short-channel effects, and compatibility with heterogeneous stacking uniquely position them as powerful complements to silicon-based platforms.[5-7] These attributes have driven advances in key device classes, ranging from field-effect transistors (FETs) with improved gate control to logic circuits enabled by polarity engineering.[8-10] Furthermore, they have demonstrated significant potentials in high-responsivity photodetectors and emerging neuromorphic devices, offering a crucial platform for future information processing.[11-13]

However, translating the current laboratory breakthroughs into practical high-performance integrated circuits requires precise, reliable control over the majority carrier type (*n*-type vs. *p*-type) and concentration, the cornerstones of complementary metal-oxide-semiconductor (CMOS) technology. Unlike conventional bulk semiconductors where high-energy ion implantation and diffusion processes define standard doping strategies, 2D materials are governed by distinct defect physics, electrostatics, and interface-dominated behaviors, all of which complicate classical doping paradigms. In most TMDs, the Fermi level (E_F) is strongly anchored by intrinsic point defects, such as chalcogen vacancies and/or unintentional impurities introduced during vapor-phase synthesis.[92] These native donor or acceptor states fix the as-grown carrier polarity (*e.g.*, robust *n*-type nature of MoS_2 and the ambipolar/*p*-type behavior of WSe_2), so a key prerequisite for the future device engineering is to understand the defect-driven origins of this native polarity and how it governs the electronic ground state of 2D semiconductors.

In response to these hurdles, an expanding library of doping approaches has been proposed to manipulate carrier polarity. These range from surface charge transfer and molecular dipole engineering[14-16] to remote charge transfer,[17-19] intercalation,[20,21] and atomic-lattice substitution.[22-28] While these strategies collectively demonstrate the electrical flexibility of TMDs, they also highlight critical trade-offs. For instance, surface or remote doping can effectively modulate the Fermi level and even enable rapid polarity switching, but the resulting charge states are often volatile, environment-sensitive, and spatially inhomogeneous. Similarly, while intercalation can access extremely high carrier densities and even induce structural phase transition, it remains challenging to reproduce in scalable devices and is strictly limited to multilayer systems.

In contrast, substitutional doping, where dopant atoms are incorporated directly into the covalent framework of the host lattice, has drawn particular attention as an intrinsically stable and integration-compatible route for deterministic carrier control. Building upon this foundation, substitutional "counter-doping" has emerged as a strategy of significant technological importance. It involves the intentional reversal of native carrier polarity, such as converting *n*-type MoS_2 to *p*-type via V/Nb/Ta substitution or turning WSe_2 into *n*-type via Re incorporation.[93,94] Counter-doping not only overcomes the defect-determined Fermi level positions but also provides a solid framework for realizing complementary logic, low-

View Article Online
DOI: 10.1039/D5NR05242D

resistance contacts, and advanced device architectures within a single-TMD platform.

This mini-review therefore aims to unify the defect physics, doping mechanisms, and device-level implications of carrier-type control in 2D TMDs. We first clarify the defect-driven origins of native carrier polarity in 2D TMDs, summarizing recent insights into how specific vacancies, antisites, and unintentional impurities generate characteristic defect states. We then survey the full spectrum of doping strategies proposed for 2D semiconductors and evaluate their respective advantages and limitations. Particular emphasis is placed on substitutional counter-doping, which enables the reprogramming of native conduction types while simultaneously allowing tunable control of carrier concentration. We further examine key demonstrations where doping-driven polarity engineering enables essential functions, including CMOS logic, *p*-*n* junctions, and reduced contact resistance, as well as emerging optoelectronic and neuromorphic applications. Finally, we outline critical remaining challenges, such as dopant activation efficiency, interfacial coupling effects with substrate and dielectrics, and the need for wide-range carrier density modulation, providing an outlook for reliable and commercially viable 2D TMD electronics.

2. From Intrinsic Defects to Intentional Doping

2.1 Native Carrier-Type and Its Defect-Driven Origins

Ideally, pristine 2D semiconductors would behave as intrinsic materials with the Fermi level positioned near the middle of the bandgap. In reality, however, the electronic ground state of most 2D TMDs (both as-synthesized or as-exfoliated specimen) is defined by unintentional doping arising from intrinsic point defects, inevitably generated in a thermodynamic aspect.[46] Beyond structural defects, the atomically thin nature of 2D materials renders them hyper-sensitive to surface absorbates/impurities. In this section, we examine the defect-driven mechanisms governing native carrier polarity in 2D semiconductors, focusing on the prototypical cases of MoS_2 and WSe_2. We aim to clarify why MoS_2 almost universally exhibits robust *n*-type behavior, whereas WSe_2 typically shows *p*-type or ambipolar conduction. Building on these insights, we further provide the physical baseline for the defect-engineering counter-doping approaches discussed in sequent chapters.

2.1.1 MoS_2: A Prototypical Intrinsic n-Type Semiconductor

The ubiquitous intrinsic *n*-type conductivity of MoS_2 is widely attributed to unintentional doping induced by sulfur vacancies (V_S).[29-31] During chemical vapor deposition (CVD), MoS_2 is typically grown at elevated temperatures under a sulfur-deficient partial pressure, conditions that thermodynamically favor the formation of anion vacancies at relatively high densities.[77,78]

From a thermodynamic perspective, the formation energies of intrinsic point defects in TMDs provide a quantitative basis for this tendency. Density functional theory (DFT) calculations consistently show that among common intrinsic defects in MoS_2 including sulfur vacancies (V_S), molybdenum vacancies (V_{Mo}), and sulfur divacancies (V_{S2}), the single sulfur vacancy has the lowest formation energy (Table 1). Specifically, the formation energy of an isolated single sulfur vacancy is reported in the range from 2.5 to 3.6 eV, which is substantially lower than

that of V_{Mo} (6.9–7.1 eV) and V_{S2} (4.3 eV).[29-31] This energetic hierarchy dictates that V_S is the dominant native defect species under typical growth conditions.

The removal of S atom leaves three under-coordinated Mo atoms with unsaturated bonds, giving rise to donor-like defect states located just below the conduction band minimum (CBM). Following thermally assisted ionization at room temperature, these defect levels increase the free electron density and accordingly drive the Fermi level toward the CBM, defining the robust *n*-type polarity of MoS_2.

Host-TMD	Defect Type	Formation energy (eV)	Role / Electronic Character	Ref.
MoS_2	V_S	2.5–3.6	Dominant donor	[29]
	V_{S2}	4.3	Deep trap	[31]
	V_{Mo}	6.9–7.1	Deep acceptor	[30]
WSe_2	V_{Se}	2.1–2.7	Deep donor / trap	[29,32]
	V_W	4.4–4.6	Acceptor-like	[32]
	$O_{Se} + V_W$	2.5–3.0	Shallow acceptor	[32]

**Note: Formation energy values are presented as ranges to account for variations in theoretical results arising from the different computational methodologies employed in cited literature.*

Table 1. Formation energies and electronic roles of representative intrinsic defects in MoS_2 and WSe_2.

2.1.2 WSe_2: Intrinsic p-Type Characteristics and Ambipolar Behavior

In contrast, WSe_2 commonly exhibits ambipolar or weakly *p*-type conduction, reflecting a fundamentally different balance of defect physics compared to MoS_2. While selenium vacancies (V_{Se}) are also among the lowest-energy native defects in WSe_2 under chalcogen-poor conditions (2.1–2.7 eV), their electronic impact is markedly different. Rather than forming simple shallow donors, the defect levels associated with V_{Se} tend to reside deeper within the bandgap and act as deep donor-like centers that do not fully ionize at room temperature.[29,32] Consequently, V_{Se} can capture electrons and contribute to mid-gap states, which do not effectively supply free carriers to the conduction band. Instead, they tend to pin the Fermi level near mid-gap and promote charge compensation, suppressing *n*-type behavior.

At the same time, W vacancies, Se-on-W antisites, and certain impurity complexes can introduce acceptor-like states closer to the valence band maximum (VBM), favoring hole population or charge compensation. Recent theoretical and experimental studies suggest that more complex defect-impurity interactions may govern the polarity of WSe_2. In particular, oxygen impurities inherent the growth environment can be incorporated to substitute for selenium (O_{Se}) and couple with adjacent tungsten vacancies (V_W), forming defect complexes

(O_{Se} + V_W) with a reduced formation energy (2.5–3.0 eV).[32] These complexes introduce shallow acceptor states close to the VBM and thereby leading *p*-type conduction. Such findings underscore that the native *p*-type or ambipolar nature of WSe_2 may not be determined solely by elemental vacancies but can also be further influenced by extrinsic impurities. In addition, because the VBM of WSe_2 aligns favorably with high-work-function metals, hole injection is generally more efficient. In contrast, its conduction band is positioned farther from the metal work function, making electron injection more sensitive to gate-induced band bending and dielectric environment. Therefore, variations in contact conditions, substrate screening, or electrostatic gating can shift the balance between electron and hole injection. Consequently, nominally "undoped" WSe_2 can display a wide spectrum of conduction behavior from predominantly *p*-type to nearly symmetric ambipolar transport across different samples and device platforms.

Understanding and controlling this defect-driven variability is crucial, as it not only dictates the native polarity of each TMD but also establishes the physical baseline from which all intentional doping and defect engineering strategies must operate.

2.2 From Intrinsic Defect Control to Intentional Doping

2.2.1 Defect Engineering Strategies and Limitations

Building on the intrinsic defect landscape discussed in Section 2.1, a natural next step has been to deliberately manipulate these defects to tune carrier polarity and density. As illustrated in Fig. 1, such "defect engineering" approaches aim to convert the unavoidable presence of defects from a liability into a design parameter for electronic functionality. Importantly, however, many of the defects generated by plasma, particle irradiation, or other strong external stimuli are off-equilibrium configurations, distinct from the thermodynamically favored native defects described in the previous chapter.

One approach involves intentionally generating chalcogen vacancies near the contact interface. For instance, controlled H_2/He plasma treatment at predefined contact regions can generate a high density of V_{Se} in WSe_2 at the contact interface (Fig. 1a). V_{Se} accumulation at the contact leads to substantial surface potential modulation. In this interface, the conduction band edge locally approaches the Fermi level with reducing electron injection barrier, resulting in a "degenerate *n*-like" contact behavior depending on the contact metal. As a result, the ambipolar *p*-branch conduction is strongly suppressed and the device shows enhanced *n*-branch on-current and reduced substhreshold swing (Fig. 1b).[33] On the other hand, vacancy healing through oxygen-incorporated CVD offers *p*-type doping pathway for carrier modulation. Shen *et al.* reported that introducing trace oxygen during CVD growth of monolayer MoS_2 (Fig. 1c,d) enables substitution of sulfur vacancies with oxygen atoms, forming Mo–O bonds that effectively passivate donor-like in-gap states. This atomic-scale oxygen healing mechanism suppressed unintentional *n*-type doping of S vacancies (Fig. 1e,f), resulting in a Fermi level downshift with reduced the metal/MoS_2 Schottky barrier to below ~40 meV.[34] Later, Zhang *et al.* extended this approach to a wafer-scale oxygen-assisted growth-repair process,

View Article Online
DOI: 10.1039/D5NR05242D

quantitatively reducing S vacancy density by an order of magnitude (from ~2.7 × 10^{13} to 4.3 × 10^{12} cm^{-2}) while simultaneously enhancing carrier mobility and lowering Fermi-level pinning.[79] Their combined results highlight that controlled oxygen healing over S vacancies not only suppresses defect-injected electron doping but also improves interface energetics and transport uniformity.

Beyond static defect creation or healing, photo-induced defect engineering has emerged as a non-contact and reconfigurable approach for carrier control. Illumination of distinct photon energies can reversibly tune carrier polarity in $MoTe_2$ through photon-driven defect chemistry: high-energy photons (≈2.4 eV, 520 nm) break Te–Te bonds to generate Te interstitials, which donate electrons and induce *n*-type conduction, whereas lower-energy light (≈1.5 eV, 830 nm) promotes oxygen substitution at Te vacancies, resulting in *p*-type doping with enhanced hole density. Such light-driven defect transformations demonstrate the dynamic tunability of intrinsic defects and highlight the potential of optical stimuli for controllable carrier modulation in 2D semiconductors.[16]

Despite these achievements, intrinsic-defect tailoring—whether by injecting chalcogen vacancies, healing them through compensating species, or dynamically reconfiguring them through photo-induced reactions—faces inherent constraints when the goal is reliable, wide-range carrier control. Vacancy-generation techniques such as plasma, laser or ion irradiation can induce collateral lattice damage, structural disorder and remain highly sensitive to exposure conditions. Also, defect density and activation efficiency are difficult to calibrate, leading to substantial device-to-device variation and limited reproducibility. Conversely, vacancy-healing approaches, including oxygen- or chalcogen-assisted treatments can suppress donor-like states, yet they offer limited controllability over a broad carrier concentration range and are highly dependent on growth conditions such as temperature and precursor chemistry.

Therefore, these limitations highlight that while intrinsic defect engineering provides valuable insights into defect-transport correlations and localized polarity tuning, it remains insufficient as a deterministic route toward wide-range and reproducible electronic control in 2D semiconductors. In this regard, other doping approaches (*i.e.*, extrinsic and substitutional doping) should be used as a functional enabler that unlocks the broader technological potential of TMDs. These methods introduce intentional dopant species—either externally coupled or substitutionally incorporated—to provide quantitative and permanent control of carrier polarity and concentration. Such deliberate doping method transforms materials once constrained by native polarity into versatile electronic platforms, paving the way toward silicon-competitive technologies.

3. Doping Strategies for 2D Semiconductors: Mechanism and Capabilities

Several doping approaches, thus, have been developed to modulate the electrical properties of TMDs. Surface charge transfer doping, achieved by adsorbing organic molecules[14,35,36,73,75] or ultrathin films[15] directly on the TMD surface, provides a simple route to tune carrier polarity and threshold voltage. However, the transferred charges are weakly bound and highly sensitive to environmental conditions such as humidity, illumination, and vacuum level. Remote charge

View Article Online
DOI: 10.1039/D5NR05242D

transfer doping, in contrast, employs a physically separated dopant reservoir—such as molecular dopants[17,18] or gate stacks[19,37] isolated by a thin spacer—through which charges can tunnel or transfer electrostatically to the channel while minimizing interfacial disorder. This approach enables rapid and reversible carrier modulation with reduced impurity scattering, but its effect is spatially confined near the interface and typically requires continuous electrostatic biasing, rendering it unsuitable for permanent doping in integrated logic. Intercalation doping, which insert alkali metals or molecular species between TMD multilayers, can induce substantial changes in carrier density and even structural phases, but unsuitable for scalable and uniform doping.[20,21,71,72] By contrast, substitutional doping, which incorporates dopant atoms directly into the TMD lattice, achieves reproducible carrier control in precision with integration-compatible manner.[22-28] Because dopants are chemically bonded within the host framework, this method offers long-term stability and scalability, allowing the functionalities in a more permanent, uniform, and technologically transferable form.

In the following sections, we review the progress of various doping approaches in 2D TMDs with their doping mechanisms and outline their advantages and limitations. Particular emphasis is placed on substitutional doping as the most robust and durable route for functionalizing 2D TMDs. We further discuss how this approach enables counter doping to reprogram carrier polarity and highlight representative demonstrations that extend such strategies into functional electronic, optoelectronic and neuromorphic device applications.

3.1 Overview of Extrinsic Doping Approaches

3.1.1 Surface charge transfer (SCT)

Surface charge transfer (SCT) doping relies on interfacial electron exchange between two materials with mismatched Fermi levels, enabling modulation of carrier polarity in 2D TMDs without altering their lattice composition. When electron-donor or -acceptor species are adsorbed directly on the atomic surface, charge transfer occurs through molecular orbital overlap or dipole formation, shifting the Fermi level of the underlying TMD channel toward the conduction or valence band. As illustrated in Fig. 2, various thiol-based and aromatic molecular systems have been employed to realize such carrier modulation through interfacial dipole engineering.

Early demonstrations using molecular dopants revealed effective polarity conversion via simple surface adsorption. Fan *et al.* achieved reversible $n \leftrightarrow p$ switching across a broad set of TMDs across MoS_2, $MoSe_2$, $MoTe_2$, WS_2 and WSe_2 by introducing boron-based donor (triphenylboron, TPB) and strong acceptor (TPB/BCF mixture) molecules, with threshold-voltage shifts (typically ≈ 10–20 V) and changes in ambipolar transport, with I_{on}/I_{off} ratios in the 10^3–10^5 range.[14] Similar molecule-induced modulation was reported by Jeong *et al*., who used 1-butanethiol (BuSH) in a mild vapor-phase treatment to heal Te vacancies in $MoTe_2$ (Fig. 2a) and shift transport toward hole conduction with a 2-order hole current increase and $\mu_h \approx 7$ $cm^2V^{-1}s^{-1}$ (Fig. 2b).[35] Im *et al*. employed bifunctional thiophenol derivatives using 4-aminothiophenol (4-ATP, donor) and 4-nitrothiophenol (4-NTP, acceptor) to tune surface

View Article Online
DOI: 10.1039/D5NR05242D

dipoles and reduce *n*-type conduction under acceptor functionalization.[36] As summarized in Fig. 2c-e, electron-donating 4ATP drives a upward Fermi level shift, whereas electron-withdrawing 4NTP pull E_F downward, reinforcing *p*-type behavior. Zhang *et al.* expanded this concept to thickness-dependent charge transfer doping in both monolayer and multilayer MoS_2 using redox-active molecules, achieving ambipolar modulation in monolayer and metallic-like transport in multilayer without structural degradation.[73] Jung *et al.* further developed a wafer-scale solution-based redox doping method using naphthalene (donor) and WCl_6 (acceptor), realizing high mobilities ($\mu_e \approx 332, \mu_h \approx 32$ $cm^2V^{-1}s^{-1}$) and on/off ratios of 10^7, with uniform band alignment control across centimeter-scale films.[75] Beyond Mo-based systems, Ji *et al.* showed that diazonium (4-NBD) and amine (DETA) molecules can reliably convert CVD-grown monolayer WSe_2 from ambipolar to *p*- and *n*-type conduction, while simultaneously improving mobility up to ~82 $cm^2V^{-1}s^{-1}$ (holes) and ~25 $cm^2V^{-1}s^{-1}$ (electrons) through enhanced injection and reduced contact resistance.[83] These results highlight that charge transfer doping through molecules provides a simple, non-destructive and chemically versatile approach. But, the physisorbed nature of molecular dopants limits their long-term environmental stability—motivating the development of more robust and interface stable doping methods.

To overcome the instability and nonuniform coverage of molecular adsorbates, Zhang *et al.* developed a template-assisted dry-transfer doping method.[15] Photolithographically patterned dopant films—Magic Blue (tris(4-bromophenyl)ammoniumyl hexachloroantimonate, strong *p*-type oxidant) and N-DMBI (1,3-dimethyl-2-phenyl-2,3-dihydro-1H-benzoimidazole, *n*-type reductant)—were dry-transferred onto $MoTe_2$, producing clean, spatially selective interfaces. This method enabled patterned and polarity-selective doping of $MoTe_2$, producing threshold-voltage shifts of approximately ± 20 V and carrier density variation in the 10^{12}–10^{13} cm^{-2} range, while preserving field-effect mobility comparable to pristine devices. The solvent-free process and photolithographic compatibility indicate potential scalability in SCT doping method for integrated device architectures.

3.1.2 Remote charge transfer (RCT)

Unlike SCT, which relies on direct contact between dopants and the 2D semiconductors, remote charge transfer (RCT) doping spatially separates the dopant source from the active channel through an ultrathin vdW dielectric spacer or an engineered gate stack. This spatial decoupling allows efficient charge transfer via tunneling or electrostatic coupling while mitigating ionized-impurity scattering at the channel. Therefore, this approach enables carrier injection with preserving interfacial cleanliness and structural integrity of 2D lattice.

Following this concept, two distinct regimes of RCT doping have been demonstrated depending on the nature of the charge reservoir as summarized in Fig. 3. In the molecule-mediated regime as the charge reservoir, Jang *et al.* introduced an ultrathin h-BN spacer (≈ 1-2 nm) between monolayer MoS_2 and a benzyl viologen (BV) donor layer (Fig. 3a). Despite the physical separation, efficient *n*-type transfer occurred because the Fermi level offset between the BV donor ($E_F \approx -4.0$ eV) and MoS_2 conduction band ($E_C \approx -4.2$ eV) created a strong built-in electrical field across the h-BN spacer, driving field-assisted tunneling of electrons into the MoS_2 channel.[17] This h-BN layer, thus, served a dual function—acting as an

View Article Online
DOI: 10.1039/D5NR05242D

electrostatic controller that modulates charge transfer strength and as a physical barrier that screens ionized-impurity scattering (Fig. 3b,c). Therefore, when increasing h-BN thickness, the transfer curve shows diminution of electron doping (Fig. 3d-f), indicating the tunneling-distance dependence in RCT doping. Building upon this principle, Lee *et al.* employed triphenylphosphine (PPh_3) molecules as remote electron donors in a WSe_2/h-BN/MoS_2 heterostructure, where the PPh_3 layer on WSe_2 acted as a charge reservoir and electrons were transferred across a few-layer h-BN dielectric (~3 nm) into the underlying MoS_2 channel. The built-in potential across the insulating spacer enabled effective *n*-type doping of MoS_2 while preserving its chemical integrity, resulting in significantly enhanced carrier transport. The remotely doped transistors showed nearly a two-fold enhancement in carrier mobility compared with directly-doped devices, indicating the effective suppression of impurity scattering across the dielectric barrier.[18] These results demonstrate that placing molecular dopants outside the active channel, in combination within and ultrathin insulating spacer, enables efficient and clean charge transfer through electrostatic coupling while preserving the intrinsic transport characteristics of the 2D semiconductors. Peng *et al.* demonstrated a spatially programmable doping strategy in $MoTe_2$ by employing patterned BV and 1,3,5-tris(4-bromophenyl)benzene (TBB) molecular layers as electron donor and acceptor species, respectively. These molecular charge reservoirs created locally distinct carrier densities, forming in-plane graded *p-n* junctions within a single $MoTe_2$ channel. The doping strength and junction profile could be dynamically modulated through external gate bias, enabling polarity switching, reconfigurable logic, and neuromorphic behaviors in the same device. The system exhibited rectification ratio up to 10^4 and synaptic responses with energy consumption as low as 7.3 fW.[19] It demonstrates that molecule-mediated charge transfer, when spatially engineered, can produce continuous carrier gradients and reconfigurable device functionality.

In contrast, the dielectric-mediated regime relies purely on electrostatic field coupling without using molecular dopants. Guo *et al.* demonstrated a Mott-interface-mediated RCT mechanism using a MoS_2/CrOCl heterostructure, where CrOCl—an antiferromagnetic Mott insulator—acts as a correlated charge reservoir (Fig. 3g). Owing to the high work function and localized 3d states of CrOCl, electrons are partially transferred from MoS_2 into the Cr 3d orbitals, producing nonlocal charge distribution and hole accumulation in MoS_2. This interfacial coupling reconfigures the channel polarity from *n*-type to *p*-type without introducing dopants or defect states, yielding hole mobilities up to ~425 $cm^2V^{-1}s^{-1}$ and on/off ratios > 10^6 that remain air-stable for over a year (Fig. 3i,j). Leveraging this vdW polarity-engineering, they demonstrated vertically integrated complementary logic (Fig. 3h,k)—inverters (6 vdW layers), NAND and SRAM circuits (14 vdW layers)—showing a pathway toward 3D integration of 2D complementary metal-oxide semiconductor (CMOS) architectures through field-coupled Mott interfaces.[37]

These findings establish that RCT doping provides a non-invasive route for carrier-type control while preserving the structural and chemical integrity of 2D semiconductors. The spatial decoupling between dopant source and conduction channel minimizes impurity scattering and interfacial disorder, preserving intrinsic transport and enabling precise polarity control. However, it is hard to realize atomically clean interfaces, stable interlayer coupling, and durable electrostatic integrity in practical process. Moreover, most of RCT methods still rely

View Article Online
DOI: 10.1039/D5NR05242D

on external molecular reservoirs or adjacent functional layers as charge sources, underscoring incomplete chemical independence. Overcoming these limitations will be essential for establishing RCT doping as a robust, wafer-scale platform for 3D integration of 2D complementary electronics.

3.1.3 Intercalation

Intercalation offers a unique means of electronic modulation in vdW solids by inserting guest species—ions, atoms, or molecules—into the interlayer vdW gaps without disrupting the basal lattice. Unlike SCT or RCT method, intercalation directly alters the host electronic configuration through charge transfer and lattice distortion. As summarized by Yang *et al*., intercalation processes can be broadly categorized into electrochemical and field-driven (electrostatic) regimes. The electrochemical route involves redox reactions and ion diffusion through liquid or solid electrolytes, enabling extremely high carrier densities ($>10^{14}$ cm^{-2}) and even superconducting states in alkali-metal intercalated TMDs. In contrast, field-driven intercalation relies on electric-field-assisted ion insertion under strong interfacial fields (~10 $MVcm^{-1}$), providing reversible and non-destructive control of charge density and lattice configuration.[20]

Building upon these principles, Gong *et al.* demonstrated precise electronic modulation of 2D SnS_2 through controlled intercalation of transition metals. Using solvent-mediated intercalation of Cu and Co atoms into the vdW gaps of bilayer SnS_2, the authors achieved deterministic conversion of carrier type and conductivity within a single crystalline lattice. Cu intercalation introduced partial charge withdrawal from SnS_2, producing *p*-type behavior with a hole mobility of ~40 $cm^2V^{-1}s^{-1}$ and I_{on}/I_{off} ratio of ~10^4, whereas Co intercalation generated strong hybridization between Co 3d and SnS_2 orbitals, driving the materials into a metallic state with a sheet resistance of ~400 Ωcm^{-1}. Crucially, the process preserved the layered structure and enabled lithographically patterned intercalation, forming in-plane *p-n* junction and *p*-type semiconductor-metal junctions with atomically sharp interfaces.[21] Shin *et al.* demonstrated that Li intercalation can also serve as an efficient interface engineering tool rather than merely a bulk doping method. By inserting Li^+ ions into multilayer WSe_2, the interfacial contact resistance was reduced via Schottky-to-ohmic transition, and the field-effect mobility was enhanced by nearly an order of magnitude (Fig. 4a-c).[85] Extending this concept to ionic species, Zhang *et al.* reported reversible and selective ion intercalation through top surface of few-layer MoS_2 (Fig. 4d,e).[71] In-situ Raman and optical spectroscopy revealed a gradual 2H→1T' phase evolution accompanied by carrier-density modulation exceeding 10^{14} cm^{-2}, evidencing intercalation-driven electronic tunability within an intact vdW lattice. More recently, Kwon *et al*. demonstrated field-programmable bimodal switching in a hybrid-dual-gated MoS_2 transistor, integrating electrostatic and intercalation doping within a single platform.[72] Under low gate bias, the device operates in a conventional electrostatic regime, while higher ionic-liquid gate voltages trigger field-driven cation insertion into the vdW gaps. This transition yields a reversible 2H→1T phase conversion and over two orders of magnitude reduction in channel resistance, confirming voltage-controlled intercalation as a non-volatile and yet recoverable doping mechanism.

Intercalation doping enables direct modulation of carrier concentration through controlled

View Article Online
DOI: 10.1039/D5NR05242D

insertion of guest species into vdW gaps, allowing access to degenerate charge densities and phase-tunable electronic states within a crystalline framework. Its reversible and spatially selective nature make it particularly suitable for defining local junctions and programmable carrier gradients in 2D materials. However, the process is inherently difficult to scale up and make precise/wide-range control of carrier concentration. Also, monolayer 2D materials cannot accommodate intercalants because interlayer gaps are required, restricting applicability to few-layer or bulk systems. In addition, chemical and structural stability can degrade due to ion migration or residual redox activity, and the use of liquid or ionic electrolytes poses compatibility issues with standard device fabrication.

3.2 Substitutional Doping and Counter-Doping: The Core of Functional Control

3.2.1 Fundamental Mechanisms and Synthesis Routes

Previously discussed extrinsic doping approaches such as surface adlayer, remote charge doping, and intercalation modulate carrier polarity and concentration primarily through interfacial or interlayer interactions, generally without permanently altering the lattice. In contrast, substitutional doping directly reconfigures the electronic ground state of the crystal and provide a path toward robust, permanent, and scalable carrier-type control. That is, through replacement of host atoms with dopant species, this approach enables deterministic control over both carrier type and concentration within the preserved crystalline framework.

In this approach, host atoms within the crystal lattice are replaced by foreign dopant species at either the transition metal (M) or chalcogen (X) sites. As illustrated in Fig. 5a, a diverse library of elements from the periodic table can be employed as substitutional dopants, encompassing various transition metals for the M-site and group 15-17 elements for the X-site. The electronic behavior of the dopant is primarily determined by its valence electron configuration relative to the host atom. For instance, replacing group-6 metals (*e.g.,* Mo, W) in MX_2 compounds with group-5 dopant (*e.g.,* V, Nb, Ta) introduces acceptor states that promote *p*-type conduction, while group-7 dopants (*e.g.,* Re) generally act as donors, driving *n*-type behavior. Beyond simple valence rules, the thermodynamic stability of dopants within the host lattice—quantified by their formation energies—strongly influences feasibility. Density functional theory (DFT) calculations have been instrumental in this regard, identifying, for example, Nb and Ta as stable *p*-type dopants in WSe_2 and Re or Cu as possible *n*-type dopants.[38,39] Such predictions not only clarify fundamental mechanisms of dopant stability but also guide experimental efforts toward viable doping strategies.

Achieving reliable substitutional doping primarily requires the incorporation of dopant atoms during growth, where precursor and reaction conditions are precisely regulated to embed dopants at lattice sites with desired concentration. Among the various bottom-up synthesis techniques, CVD remains the most widely employed,[24-27] offering controllable growth kinetics (Fig. 5b,c). By modulating precursor ratios, substrate temperature, and carrier gas composition, dopant incorporation can be tuned from dilute to degenerate levels while maintaining crystal continuity. Metal-organic chemical vapor deposition (MOCVD) further enhances this controllability by utilizing volatile organometallic precursors,[45,86,88] enabling precise

View Article Online
DOI: 10.1039/D5NR05242D

adjustment of dopant flux and spatial uniformity and scalability (Fig. 5d). In addition to vapor-phase methods, as shown in Fig. 5e, magnetron co-sputtering combined with post-chalcogenization has recently emerged as a promising solid-gas hybrid route.[22] Here, dopant atoms are alloyed with host-metal precursors in a sputtered film prior to chalcogen reaction, allowing near-stoichiometric substitution and fine doping resolution at relatively low temperatures. This approach provides enhanced integration compatibility with pre-patterned substrates. On the other hand, chemical vapor transport (CVT) enables thermodynamically equilibrated incorporation of dopants during bulk single-crystal growth, yielding high-purity doped-single crystals that can be exfoliated into few-layer flakes for fundamental property assessment (Fig. 5f).[28,80,87]

Beyond these methodological distinctions, the advantages of substitutional doping are rooted in its intrinsic robustness and chemical stability. Once incorporated, dopants form covalent bonds with the host lattice, ensuring long-term durability even under ambient exposure and elevated temperatures. This permanence contrasts sharply with other extrinsic approaches such as molecular adsorption or intercalation, which are typically volatile and unsuitable for reliable device operation. In addition, bottom-up synthesis methods such as CVD and MOCVD provide a practical route to reproducible and scalable incorporation, enabling spatially uniform dopant distribution and tunable concentrations across wafer-scale. These attributes make substitutional doping uniquely positioned to bridge laboratory demonstrations with industrial integration. Table 2 presents representative experimental demonstrations of substitutional counter-doping in various TMDs, summarizing a diverse array of dopants and host lattice combinations.

While substitutional incorporation offers such advantages, it also faces several practical and scientific challenges. The thermodynamics of dopant substitution are often limited by low solubility and competing phase formation, leading to unintended alloying or defect clustering. Additional challenges of substitutional doping will be discussed in detail in Section 4 (Outlook). In the following subsections, we highlight representative case studies that overcome these limitations of doping chemistry and realize well-defined *p*-type and *n*-type doping conduction in 2D TMDs with specific dopant species.

3.2.2 p-Type Doping: V, Nb, Ta

Vanadium (V) Substitution In 2H-MoS_2, molybdenum typically adopts the +4 oxidation state (Mo^{4+}, $4d^2$). When Mo^{4+} is replaced by group-5 metals such as V^{4+} ($3d^1$), the one-electron deficiency introduces shallow acceptor states near VBM, driving a downward shift of the Fermi level and establishing *p*-type conduction. Zou *et al.* achieved controllable V doping into monolayer MoS_2 by CVD using variable precursors (*e.g.*, V_2O_5, NH_4VO_3, VCl_3), realizing substitutional doping from 0.3 to 13.1 at%.[25] Zhang *et al*. demonstrated quasi-continuous control of carrier polarity in monolayer MoS_2 by V doping through CVD method (Fig. 6a,b) from intrinsic *n*-type through ambipolar to degenerate *p*-type transport. DFT calculations correlated the observed ~1 eV Fermi level downshift with shallow acceptor formation and upward movement of the valence band edge.[74] Because the covalent radii of Mo and V (154 vs 153 pm) and their lattice constants ($a \approx 3.18$ Å) are nearly identical, substitution proceeds with low strain and high solubility with continuous electronic tunability. Optical and transport investigations by Zheng *et al.* further confirmed the *p*-type character, revealing doping-induced

View Article Online
DOI: 10.1039/D5NR05242D

band-gap narrowing and a pronounced enhancement of the B-exciton emission in V-doped MoS_2. HAADF-STEM images clearly show V incorporation in Mo sites (Fig. 6c), and their optical results reflect reduced spin-orbit splitting and efficient exciton-valley scattering, both arising from hole accumulation and mild lattice distortion around V sites.[76]

Niobium (Nb) Substitution Because W and Nb have comparable covalent radii (Nb: 134 pm, W: 137pm) and similar lattice parameters, Nb can be easily incorporated into 2H-WS_2 with minimal strain and high solubility. When W^{4+} ($5d^2$) sites are replaced by Nb^{4+} ($4d^1$), the one-electron deficiency generates shallow acceptor states near VBM, shifting Fermi-level downward, inducing *p*-type conduction. Tang *et al.* achieved controllable Nb doping in monolayer WS_2 by CVD using mixed $WO_3/NbCl_5$ precursors (Fig.6d), realizing doping concentration from ~0.3 to 4.7 at%.[40] Systematic redshifts in photoluminescence (PL) and core-level binding energy decreases in X-ray photoelectron spectroscopy (XPS) verified band-gap narrowing and Fermi level lowering by acceptor formation (Fig.6e-g). Consistent optical and XPS trends were also observed in Nb-doped WS_2 by Zhang *et al.*,[84] further supporting that such PL redshifts and core-level shifts are characteristic signatures of acceptor-induced Fermi level lowering. Qin *et al.* further realized substitutional Nb doping via liquid-phase precursor mixing, where atomic-resolution high-angle annular dark-field scanning transmission electron microscopy (HAADF-STEM) directly visualized Nb atoms at W sites and transport characteristics evolved from *n*-type through ambipolar to *p*-type with increasing Nb concentration.[81] Wang *et al.* demonstrated MOCVD growth of lateral NbS_2-MoS_2 heterostructures, in which Nb substitutionally incorporated into the MoS_2 domain, enabling stable *p*-type conduction and reduced Schottky barriers (~230 meV) at the interface.[45]

Tantalum (Ta) Substitution Ta, another group-5 element, offers a unique balance between chemical stability and strong acceptor behavior due to its relatively large atomic radius and strong d-p orbital hybridization with chalcogen orbitals. Li *et al.* reported one-step NaCl-assisted CVD growth of Ta-doped monolayer MoS_2, achieving substitutional incorporation up to ~1.3 at% (Fig. 6h).[26] Structural and spectroscopic analyses confirmed that the doped layers retain the pristine 2H lattice with negligible defect formation and a shift of the Mo 3d and S 2p core levels toward lower binding energies, consistent with Fermi level movement toward VBM. FETs based on Ta-doped MoS_2 exhibit clear *p*-type transfer characteristics, accompanied by positive threshold-voltage shifts and reduced subthreshold swings, evidencing efficient hole conduction through substitutional Ta acceptor states.

3.2.3 n-Type Doping: Re and beyond

Rhenium (Re) Substitution While group-5 dopants such as V and Nb effectively induce *p*-type conduction through electron deficiency, group-7 Re provides the opposite doping polarity, serving as a prototypical donor that drives Fermi-level upshift and *n*-type transport in TMDs. In WSe_2, Kozhakhmetov *et al.* reported Re substitution by MOCVD using $W(CO)_6$, H_2Se, and $Re_2(CO)_{10}$ precursors, precisely controlling dopant concentrations.[88] XPS and ToF-SIMS verified substitutional Re at W sites (Fig.6k). Also, Raman spectra showed the emergence of defect-activated LA(M) and ZA(M) modes and PL redshift/quenching (~40 meV) with increasing Re content, attributed to enhanced trion formation and electron doping (Fig. 6l,m). DFT and scanning tunnelling microscope and spectroscopy (STM/STS) measurements

revealed that Re_w donor states lying 0.1–0.4 eV below CBM with binding energies of 200–300 meV, explaining the partial ionization and deactivated carrier behavior at room temperature.

In MoS_2, Zhang *et al.* achieved in-situ substitutional Re incorporation via CVD growth using ReO_3 in MoS_2 up to 1 at% (Fig. 6i).[27] Atomic-resolution STEM confirmed Re atoms replacing Mo sites (Fig. 6j), and XPS showed the VBM shifting from 1.4 to 1.9 eV below E_F, indicating Fermi-level upshift toward the CBM. Also, PL red-shifted and quenched (~ 30 meV), consistent with enhanced and *n*-type doping. Torshi *et al.* later extended this to dilute regimes (< 0.1 at%) via MOCVD, precisely tuning Re supply from $Re_2(CO)_{10}$. XPS and time-of-flight secondary ion mass spectrometer (ToF-SIMS) verified substitutional Re, and PL revealed progressive quenching of defect-related emission with higher Re concentration. The reduction of Mo-O defect peaks and shortened carrier lifetime components indicated electron donation and vacancy passivation.[41]

Dopant	Host-TMD	Doping method	Dopant Precursor	Doping Range	Type	Device Behavior	Ref.
V	MoS_2	CVD	V_2O_5, NH_4VO_3, VCl_3	0.3–13 at%	P	Synaptic transistor	[25]
V	WS_2	CVD	VCl_3	≤ 1 at%	P	p-n phototransistor array	[24]
Nb	WS_2	CVD	$NbCl_5$	0.3–4.7 at%	P	Polarity conversion	[40]
Nb+Re	$MoTe_2$	Co-sputtering + tellurization	-	0.06–0.42 at%	P, N	CMOS inverter array	[22]
Ta	MoS_2	CVD	$TaCl_5$	≤ 1.3 at%	P	Stable *p*-channel	[26]
Re	MoS_2	CVD	ReO_3	≤ 0.8 at%	N	Fermi level upshift	[27]
Re	WSe_2	MOCVD	$Re_2(CO)_{10}$	<0.001–0.1at%	N	Wafer-scale doping	[88]

Table 2. Representative substitutional counter-doping demonstrations in 2D TMDs.

Beyond Group-7: Cobalt (Co) and Iron (Fe) Substitution While group-7 elements like Re are utilized for electron donation, introducing other transition metals can further expand the functional capabilities of TMDs, particularly by inducing magnetic moments into the semiconducting framework. Co and Fe substitution have emerged as key method for creating 2D dilute magnetic semiconductors, where internal magnetic moments couple with the host's electronic structure to enable magnetic control.

Co substitution in MoS_2 has been shown to serve as an effective means to engineer valley

View Article Online
DOI: 10.1039/D5NR05242D

Zeeman splitting (VZS). Zhou *et al.* reported the successful Co-doped MoS_2 monolayers with different doping concentration by CVD process.[95] The atomic resolution STEM identified two distinct configurations, which is isolated single dopants and tridopant clusters. While isolated Co atoms contribute to localized bonding, the tridopant clusters that consist of three Co atoms surrounding with central S vacancy induce an internal magnetic field through ferromagnetic coupling. This internal field couples to the spin, atomic orbital, and valley magnetic moments, resulting in a high enhancement of VZS with Landé g-factors up to ~15, significantly exceeding pristine monolayers.

Likewise, Fe substitution shows a similar pathway toward achieving robust magnetic order. Fe atoms can be incorporated into MoS_2 monolayer by CVD growth and this substitution can be confirmed by Fe-related radiative PL emissions at 2.28 eV.[96] Notably, spatially resolved magnetometry and superconducting quantum interference device measurements have demonstrated that Fe-doped MoS_2 monolayers have clear ferromagnetism at room temperature, showing M-H hysteresis loops. These results demonstrate that substitutional doping beyond group-7 elements can also show the promise for advanced spintronic and magnetic applications.

4. Device-Level Application Enabled by Controlled Doping

While diverse doping strategies have been explored to modulate the carrier polarity of TMDs, their ultimate significance is defined by how effectively they translate into device-level functionality. Building on the concept of counter doping and polarity reversal discussed earlier, recent efforts have demonstrated that controlled doping enables not only carrier-type reprogramming but also the realization of practical device architectures. These applications can be broadly grouped into two domains. Within the CMOS paradigm, doping has been employed to construct complementary logic inverters, high-quality *p*-*n* junction diodes, and low-resistance ohmic vdW contacts, thereby addressing integration challenges. Beyond CMOS applications, doping also opens pathways to optoelectronic devices with enhanced responsivity and to neuromorphic platforms capable of emulating synaptic plasticity. The following sections examine these developments, highlighting how doping strategies of varying nature coverage enables next-generation device functionality in TMDs.

4.1 CMOS device applications

4.1.1 CMOS logic and inverters

Recent advances have demonstrated that substitutional counter-doping can surpass simple polarity modulation and directly translate into functional circuit-level integration. Unlike SCT or RCT methods, which are often volatile and spatially restricted, atomically incorporated dopants provide robust and compatible complementary channels suitable for large-area 2D logic. Therefore, Gao *et al.* reported V-doped monolayer WS_2 as a platform for CMOS inverters.[42] Controlled substitution of V at W sites during CVD growth modulated the carrier polarity continuously from *n*-type to *p*-type as the dopant concentration increased to 4.7 at%. By integrating *p*-type 4.7 at% V-doped WS_2 and pristine *n*-type WS_2 flakes on same substrate, they demonstrated inverters with Ni contacts for *p*-FET and Au for *n*-FET (Fig. 7a). The voltage transfer characteristics and corresponding gain were obtained under different voltage (V_{DD} = 1,3,5V), showing stable logic inversion and well-balanced output between the

View Article Online
DOI: 10.1039/D5NR05242D

complementary branches (Fig. 7b,c). Similarly, Pan *et al.* demonstrated complementary logic in 2H-$MoTe_2$ through precisely controlled substitutional doping with Nb and Re as acceptor and donor species, respectively.[22] By co-sputtering Nb or Re into Mo precursor films followed by CVD tellurization, they made few-layer 2H-$MoTe_2$ with tunable carrier concentrations from 10^{10} to 10^{12} cm^{-2} and confirmed *p*-type and *n*-type conduction via Hall measurements (Fig. 7d). Using lithographically defined Nb- and Re-doped regions, patterned 2H-$MoTe_2$ channels were monolithically integrated on SiO_2/Si substrates without any transfer process (Fig. 7e). The resulting CMOS inverters, employing Pd/Au and Ti/Au contacts for *p*- and *n*-FETs, exhibited balanced saturation currents (~0.6 μA and ~0.8 μA) and clean voltage transfer characteristics with logic inversion at V_{DD} =1−4 V (Fig. 7f). The voltage gain increased from 2.6 at 1 V to 38.2 at 4 V, while the peak static power consumption arise from 1.5 nW to 89.5 nW (Fig.7g,h). Collectively, these studies establish substitutional counter-doping as a deterministic and CMOS-compatible framework for constructing stable complementary inverters in 2D materials—where dopant chemistry directly governs device symmetry, gain, and scalability.

4.1.2 p-n junction diodes

Beyond transistor-level modulation, substitutional doping provides a powerful route for forming intrinsic *p-n* junctions within a continuous 2D lattice. The resulting chemically defined junctions avoid the interfacial contamination and Fermi-level disorder often encountered in transfer-assembled heterostructures. Vu *et al.* developed Nb-doped WS_2–MoS_2 lateral heterojunctions via a solution-assisted CVD process that utilizes the different chemical reactivites of MoO_3, WO_3 and Nb_2O_5. Intrinsic MoS_2 was first grown at 700 ℃, followed by Nb-doped WS_2 at 800 ℃, where the Nb-doped WS_2 acted as *p*-type while MoS_2 domain retained its *n*-type character.[89] By adjusting the Nb/(W+Nb) molar ratio in precursor solution, the hole carrier density in WS_2 was tuned from 1.87×10^6 cm^{-2} at 1.5 at% Nb to 1.16×10^{13} cm^{-2} at 8.1 at% Nb, corresponding to a gradual transition from *n-n* to *p-n* conduction. The optimized *p-n* junction diode device exhibited a rectification ratio of ~10^5 and a specific detectivity of 1.1×10^{14} Jones under 638 nm illumination. It shows that the junction characteristics are directly governed by dopant concentration and associated Fermi level tuning.

4.1.3 Low-resistance electrical contacts

Reducing contact resistance remains one of the primary bottlenecks for high-performance 2D transistors. Recent advances in substitutional doping and 2D metallic electrode engineering have demonstrated effective strategies to achieve near-ohmic behavior and contact resistance minimization. Vu *et al.* established a one-step route to synthesize $NbSe_2$/Nb-doped WSe_2 edge-contact heterostructures, where $NbSe_2$ acts as a metallic contact grown in-situ along the edge of *p*-type WSe_2 domains (Fig. 8a,b).[43] By increasing the Nb molar ratio up to 60%, the hole density of WSe_2 channel increased from ~3×10^{11} cm^{-2} to 1.38×10^{12} cm^{-2}, and the Schottky barrier height (Φ_{SB}) was reduced from 0.34 eV (Cr/WSe_2) to − 0.68 eV ($NbSe_2$/Nb-doped WSe_2) (Fig. 8d,e). The corresponding contact resistance dropped from 10.9 MΩ μm (Cr) to 2.46 kΩ μm ($NbSe_2$), marking nearly four orders of magnitude improvement. DFT calculations confirmed that the negative Schottky barrier height originated from the higher

View Article Online
DOI: 10.1039/D5NR05242D

work function of metallic $NbSe_2$ (5.52 eV) aligning with the VBM (4.84 eV) of Nb-doped WSe_2, enabling true *p*-type ohmic contact formation. In other case, Wang *et al.* reported NbS_2-MoS_2 lateral heterostructure grown by a single-step MOCVD process.[45] The NbS_2 metallic phase served as an intrinsic 2D electrode for Nb-doped MoS_2 semiconductor, mitigating interface disorder and reducing Fermi level pinning. The resulting devices displayed linear *I-V* behavior with ohmic contact characteristics, a *p*-type on/off ratio of 10^4, and a mobility of 1.46 $cm^2V^{-1}s^{-1}$ (Fig. 8c). Quantum transport simulations revealed localized potential steps of ~72–90 meV at the $NbSe_2$/*p*-MoS_2 junction (Fig. 8f). Recently, Jiang *et al.* introduced yttrium substitution in 2H-MoS_2 as a transformative strategy for contact metallization. The plasma–deposition–annealing process replaced surface sulfur atoms with yttrium (Y), driving a controlled 2H → semi-metallic transition. The resulting Y–MoS_2 contact layers exhibited an ultralow contact resistance of 69 Ω μm and on-current densities exceeding 1.22 mA μm^{-1} in 10 nm-gate devices, all while maintaining vdW interfaces free of interdiffusion.[44] Taken together, these results collectively demonstrate that substitutional doping enables contact engineering at the atomic scale—where the boundary between semiconductor and metal is chemically encoded rather than physically deposited—thereby unifying polarity control and injection optimization within a single growth framework.

While substitutional counter-doping provides a deterministic and CMOS-compatible route for constructing complementary channels and contacts, its role in broader device classes becomes more complex. Optoelectronic and neuromorphic devices often require dynamic carrier modulation, local tuning of band edges, or gradual conductance control that cannot always be achieved through substitutional incorporation alone. In these systems, additional doping mechanisms—such as plasma-assisted surface doping, intercalation-driven Fermi level engineering, or molecular charge-transfer processes—play a complementary role by enabling reversible polarity tuning, exciton-level control, or continuous conductance modulation. Therefore, whereas substitutional doping defines a stable electronic baseline and ensures long-term structural robustness, extrinsic and field-driven doping methods provide the flexibility required for photodetection, energy harvesting, and synaptic behavior. Based on this broader landscape, recent studies have shown that a combination of substitutional and non-substitutional doping strategies can unlock enhanced optoelectronic response and neuromorphic functionalities in 2D TMDs.

4.2 Beyond CMOS device applications

4.2.1 Optoelectronics applications

Substitutional V doping in CVD-grown MoS_2 yields UV–Vis photodiodes with a responsivity approaching 978 A W^{-1} and a detectivity above 10^{13} Jones.[47] Similarly, Ta-doped $MoSe_2$ produces vertical p–n homojunction devices with $V_{OC} \approx 0.68$ V, an EQE ≈ 42%, and sub-100 μs response speed, supporting low-power and fast photodetection.[48] Uniform plasma-assisted doping has also proven effective for converting the top layers of multilayer MoS_2 into *p*-type regions, thereby forming a vertical *p-n* junction within a single flake. This approach yields a short-circuit current densities of 20.9 mA cm^{-2}, $V_{OC} \approx 0.28$ V, and a power conversion efficiency of 2.8%, together with external quantum efficiencies of 37–78% across the visible

View Article Online
DOI: 10.1039/D5NR05242D

spectrum and rectification ratios >10^4.[49]

Building on these uniform doping approaches, patterned counter-doping has been developed to locally define *p*- and *n*-type regions within a single channel. Nitrogen plasma doping of MoS_2 creates lateral *p*-*n* homojunctions exhibiting rectification ratios exceeding 10^3 and a gate-tunable photovoltaic response,[50] while low-energy nitrogen ion implantation in WS_2 produces homojunctions with an open-circuit voltages of 0.39 V and a responsivity > 10^3 A W^{-1} under AM 1.5 G illumination, highlighting their potential for wafer-scale, transfer-free photodetectors, as shown in Fig. 9a-c.[51]

Beyond junction formation, these doping strategies facilitate wafer-scale Fermi level tunning and reversible polarity control—functionalities central to high-performance photodetection and circuit integration. Notably, intercalation-based approaches enable such modulation while preserving crystalline framework. Specifically, sodium insertion into MoS_2 significantly enhances photodetector responsivity by nearly two-fold, notably without introducing significant structural disorder (Fig. 9d-f).[52] Furthermore, SCT doping allows for reversible dominant carrier conversion and precise threshold-voltage control at the circuit level. Alternating octadecyltrichlorosilane (ODTS, acceptor) and poly-L-lysine (PLL, donor) treatments enable complementary inverter fabrication using $MoTe_2$ and hetero-TMD FETs, which have been successfully employed as μ-LED display backplanes, maintaining stable current delivery and mechanical flexibility even on PET substrates.[53] These results suggest a promising route toward monolithic optical interconnects and flexible display technologies powered by counter-doped 2D semiconductors.

4.2.2 Neuromorphic and Computing applications

The continuous scaling of conventional von Neumann architectures are increasingly constrained by speed and power limitations, prompting the exploration of brain-inspired computing for next-generation information processing. By co-locating memory and computation and operating in a massively parallel, event-driven manner, neuromorphic systems promise energy-efficient learning and real-time data processing. Implementing such functionality at the hardware level requires electronic elements capable of emulating essential synaptic behaviors—including potentiation, depression, and spike-timing-dependent plasticity (STDP)—with ensuring robust scalability and reproducibility.

Crucially, counter-doping provides a versatile platform for realizing such synaptic functionalities in 2D semiconductors. Reversible carrier density modulation and Fermi level control within the same MoS_2 channel enable smooth, analog-like conductance tuning and low-power operation—key requirements for hardware-level learning rules. Nb-doped MoS_2 transistors, which function as optoelectronic reservoirs, exhibit I_{on}/I_{off} ratios exceeding 10^6, subthreshold swings of 234 $mVdec^{-1}$, and stable operation under ambient conditions, functioning as optoelectronic reservoirs. These reservoir devices achieve 100% motion recognition across eight directions and 88% pattern-recognition accuracy under sequential optical stimulation, demonstrating their promise for reservoir computing.[54] Additional demonstrations further highlight the ability of counter-doping to enable multilevel and reconfigurable conductance states. Oxygen-doped MoS_2 memtransistors demonstrate >50

View Article Online
DOI: 10.1039/D5NR05242D

stable conductance levels, long-term potentiation/depression with >10^3s retention, and highly linear weight updates, making them well suited for analog neuromorphic learning tasks.[55] Similarly, precisely controlled charge-trapping dynamics in MoS_2 FETs enable tunable excitatory and inhibitory postsynaptic currents, paired-pulse facilitation, and programmable STDP learning windows, thereby facilitating the direct implementation of Hebbian learning and temporal sequence recognition (Fig. 9g-l).[56] Together, these studies demonstrate that counter-doping serves as a practical route for implementing plastic and reconfigurable synaptic devices. The ability to engineer polarity and carrier density within a single 2D material system paves the way toward energy-efficient in-memory computing, associative learning, and on-chip spiking neural networks.

5. Outlook: Challenges and Future Opportunities

A variety of doping routes—ranging from substitutional incorporation to intercalation-based and charge-transfer processes—have broadened the toolbox for tailoring electronic behavior in 2D semiconductors. Among these approaches, substitutional doping represents the route that directly modifies the lattice and establishes a built-in carrier type. Nevertheless, several fundamental limitations still constrain the expendability and predictability of 2D doping. At the atomic level, dopant activation yield remains insufficient because of strong quantum confinement and reduced dielectric screening. At the mesoscale, dopant–interface interactions with substrates, dielectrics, and contacts can overshadow the dopant contributions and obscure the true carrier polarity set by the lattice. At the device and wafer levels, the spatial distribution of dopants is difficult to control within acceptable uniformity thresholds, and bridging the broad concentration range—from single dopant atoms to degenerate metallic phases—requires new paradigms of process modulation. This section outlines three key research frontiers that collectively define the future of 2D doping science: (1) improving dopant activation efficiency through band-edge and dielectric engineering, (2) mitigating interfacial coupling that distorts intended doping behavior, and (3) achieving continuous tunability across dilute-to-degenerate regimes. By unifying these axes, the field can progress from isolated doping demonstrations toward reproducible, designable 2D electronic systems.

5.1 Dopant Activation Efficiency

The dopant activation efficiency (η_{act}) can be generally defined as:

$$\eta_{act} = \frac{N_{ionized}}{N_{total}}$$

where $N_{ionized}$ is the concentration of ionized dopants that contribute free carriers and N_{total} is the total incorporated dopant density. If the dopants behaved as shallow-level impurities, their ionization energy can be described by the hydrogenic effective-mass model, which assumes a weak long-range Coulomb potential and a delocalized impurity state. In this idealized limit, the 2D ionization energy takes:[63]

$$E_i \approx \frac{2m^* e^4}{\left(4\pi\varepsilon_0\varepsilon_{eff}\right)^2 \hbar^2}$$

View Article Online
DOI: 10.1039/D5NR05242D

where m^* is the carrier effective mass (m_e^* for donors and m_h^* for acceptors), e is the electron charge, ε_0 is the vacuum permittivity, ε_{eff} is the effective dielectric constant, and $\hbar$ is the reduced Planck constant. In this equation, it explains that low activation efficiency is mainly due to large dopant ionization energy (E_i), which is enhanced by weak dielectric screening and strong quantum confinement in atomically thin layers. Because monolayer 2D semiconductors experience strongly reduced dielectric screening due to their atomic-thin geometry and surrounding environment (*e.g.,* vaccum, air, or low-ε dielectrics),[68,90,91] the resulting E_i can rise to 200-400 meV, exceeding k_BT at room temperature and preventing thermal ionization. Encapsulating monolayers with high-κ dielectrics (*e.g.,* HfO_2, Al_2O_3) can enhance ε_{eff} and reduces E_i, allowing more dopant to ionize thermally.

In this deep-level regime, dopant activation in 2D TMDs can be described using charge-transition-level (CTL) formalism. First-principles studies show that when their electronic levels are deep and strongly localized, they are dominated by short-range bonding and substantial lattice relaxation.

Then, the activation efficiency follows the Fermi-Dirac occupation of CTLs.[64] For acceptors:

$$\eta_{act}^{A} = \frac{1}{1 + g_A \exp\left(\frac{E_A - E_F}{k_BT}\right)}$$

with a corresponding expression for donors:

$$\eta_{act}^{D} = \frac{1}{1 + g_D \exp\left(\frac{E_F - E_D}{k_BT}\right)}$$

where g_D (g_A) is the degeneracy factor, E_D (E_A) is the dopant energy level, and E_F is the Fermi level.

These relations highlight that dopant activation in monolayer 2D semiconductors is more likely to be governed by CTL depth, defect-state localization, and lattice relaxation, rather than by the hydrogenic model applicable to bulk semiconductors or shallow dopants.

5.2 Interfacial Effects with Substrates, Dielectrics, and Contacts

Because every atom in a 2D crystal lies at an interface, intentional doping competes with electrostatic perturbations from the surrounding environment. At the substrate—semiconductor interface, trapped charges and dipoles an additional potential that can hinder the dopant effect.[65-67] The effective potential profile satisfies Poisson's equation:

$$\nabla^2\phi = -\frac{\rho_{dop} + \rho_{int}}{\varepsilon_0 \varepsilon}$$

where ρ_{dop} is the charge density from ionized dopants and ρ_{int} represents interface-trapped or fixed charges. If $|\rho_{int}| \gg |\rho_{dop}|$, doping-induced polarity becomes obscured by substrate-induced band bending.

View Article Online
DOI: 10.1039/D5NR05242D

For future device integration, interface co-design can improve the performance of doping. A hybrid "vdW spacer + high-κ" configuration (*e.g.,* h-BN/HfO_2) or vdW integration of high-κ dielectric can minimize chemical reactivity while providing strong electrostatic control.[59,60] The ultimate research goal is to develop the high-κ vdW dielectrics. Unlike bulk 3D oxides, these vdW dielectrics (*e.g.,* LaOCl, LaOBr) can be integrated without forming interfacial dangling bonds or trapped charges, thereby enhance the doping efficiency of 2D semiconductors.[57,58] This research direction is rapidly expanding, as they seek scalable synthesis routes and interface-engineered stacks that deliver high-κ screening without the parasitic effects of bulk dielectrics.

Also, another challenge in 2D semiconductor is suppression of metal-induced gap states (MIGS) and Fermi-level pinning (FLP) that typically occur when metal electrodes are deposited onto 2D channels.[69] Beyond post-deposition depinning treatments,[70] substitutional doping near the contact region to locally tune the band alignment or degenerate doping and in-plane metallic seams can act as atomically coherent electrodes and transform the semiconductor into a semimetal.

5.3 Wide-Range Doping Concentration Coverage

A future-proof 2D doping framework must cover the entire concentration spectrum—from isolated impurity states for quantum devices to degenerate metallic phases for ohmic contacts. Each regime imposes distinct physical constraints. In the dilute limit (n $< 10^{11}$ cm^{-2}), dopants act as quantum emitters[82] or charge traps whose localized states determine single-photon or spin behaviors. The stability of the charge state and spectral linewidth (Γ) under gating conditions are the key merit. Encapsulation with h-BN and defect engineering can suppress charge noise, allowing deterministic quantum control of dopant states (*e.g.,* single Re or V atoms in TMDs).

In the moderate regime (10^{12}–10^{13} cm^{-2}), which defines transistor operation, mobility degradation due to ionized-impurity scattering becomes significant. The mobility (μ) scales inversely with dopant density (N_{dop}) as

$$\mu^{-1} = \mu_0^{-1} + \frac{N_{dop} e^3 \ln \Lambda}{16\pi\varepsilon^2\hbar^2 n},$$

Where $\mu_0$is the intrinsic mobility (phonon-limited), $e$is the elementary charge, Λ is the screening length, and n is the free carrier concentration.[61] Designing dopant distributions that are shallow yet spatially smooth minimizes scattering while maintaining threshold tunability. Hybrid approaches—combining permanent substitutional doping with volatile charge modulation—could offer dynamic reconfigurability for adaptive 2D circuits.

At the degenerate regime ($n > n_c \approx m^* E_B/\pi\hbar^2$, where $E_B$is the binding energy),[62] the semiconductor undergoes a transition toward a semimetallic state. Controlled metallization, such as Y-doped MoS_2 or NbS_2–MoS_2 heterostructures, yields contact resistances below 100 Ω·μm and current densities exceeding 1 mA μm^{-1}.[44,45]

View Article Online
DOI: 10.1039/D5NR05242D

5.4 Future opportunities of doping in 2D semiconductors

Doping in 2D semiconductors has been regarded as a strategy for modulating carrier density and polarity within a fixed host lattice. While this framework has been effective for understanding *n*-type and *p*-type control in semiconducting TMDs, recent progress suggests that doping in 2D systems offers a broader design space. In particular, substitutional doping at elevated concentrations can fundamentally alter the crystal symmetry, electronic structure, and electronic phases of the host, thereby blurring the boundary between "doped materials" and entirely new host TMDs. At sufficiently high substitution levels, dopant atoms no longer act as dilute perturbations but instead define the dominant metal sublattice. For example, V-doped MoS_2 can be continuously connected to VS_2, Nb-doped MoS_2 to NbS_2, and Re-doped TMDs to ReS_2 or $ReSe_2$. Importantly, this expanded view of doping opens new opportunities for device concepts that combine doped semiconducting TMDs with intrinsically metallic or distorted TMDs. For instance, doped-TMDs may serve as channels or junction regions, while materials such as VS_2, NbS_2, or ReS_2 can function as contact, selective electrodes, or anisotropic transport layers. Such hybrid architectures could enable seamless band alignment, reduced contact resistance, and new functionalities that are difficult to achieve using conventional metal electrodes or lightly-doped channels alone. Because those compounds like VS_2 and NbS_2 naturally have high carrier densities and ReS_2 exhibits intrinsically distorted 1T' crystal structure, strong in-plane anisotropy, and weak interlayer coupling.[97,98]

Based on these considerations, a conceptual roadmap for doping-enabled 2D semiconductors technologies can be outlined as Fig. 10. In the early stage, research focused primarily on intrinsic defects, such as chalcogen vacancies, which largely determine the native carrier polarity and transport behavior of semiconducting TMDs. This period established the baseline understanding of intrinsic defect-induced doping. The current stage shows diverse extrinsic doping strategies including especially focused on substitutional doping method. It shows developments of precise doping concentration, spatial uniformity and selectivity, and various dopant elements. Such approaches enable systematic control which bridges the gap between defect-dominated behavior and dopant-defined electronic regimes. Looking forward, the doped-TMDs can be integrated into hybrid material systems and enable scalable 2D CMOS logic hubs, sensor hubs, emerging quantum platforms and flexible displays. In this overall perspective, doping evolves from a tuning parameter into a materials design.

Authors contributions

S.K. conceived the review, organized the overall structure, and wrote the manuscript with assistance of H.J. J.Y. wrote Section 3.3.2 and contributed to literature survey. J.S. supervised the manuscript preparation, provided critical revisions, and guided the overall direction of the manuscript. All authors reviewed and approved the final version of the manuscript.

Acknowledgements

View Article Online
DOI: 10.1039/D5NR05242D

This work was supported by the National Research Foundation of Korea (NRF) funded by the Ministry of Education (RS-2024-00336695, RS-2025-12602968 and RS-2025-23323754) and Samsung Research Funding & Incubation Centre of Samsung Electronics under Project Number SRFC-A2401-1 and partially supported by Samsung-UNIST Semiconductor Cluster funded by Samsung Electronics (2.250492.01). S.K. acknowledges the support from the National Research Foundation of Korea grant (2.251103.01)

Conflicts of interest

There are no conflicts to declare.

View Article Online
DOI: 10.1039/D5NR05242D

References

1. A. K. Geim and K. S. Novoselov, *Nat. Mater.*, 2007, **6**, 183–191.
2. B. Radisavljevic, A. Radenovic, J. Brivio, V. Giacometti and A. Kis, *Nat. Nanotechnol.*, 2011, **6**, 147–150.
3. D. Akinwande, C. Huyghebaert, C.-H. Wang, M. I. Serna, S. Goossens, L.-J. Li, H.-S. P. Wong and F. H. L. Koppens, *Nature*, 2019, **573**, 507–518.
4. S. Zeng, C. Liu, P. Zhou and F. H. L. Koppens, *Nat. Rev. Electr. Eng.*, 2024, **1**, 335–348
5. Y. Liu, X. Duan, H.-J. Shin, S. Park, Y. Huang and X. Duan, *Nature*, 2021, **591**, 43–53.
6. Y. Liu, Y. Huang and X. Duan, *Nature*, 2019, **567**, 323-333.
7. W. Cao, H. Bu, Y. Liu, P. D. Ye, J. P. Dimitrakopoulos, K. Banerjee and S. L. Goldstein, *Nature*, 2023, **620**, 78–87.
8. D. Jayachandran, R. Pendurthi, M. Ul Karim Sadaf, N. U. Sakib, A. Pannone, C. Chen, Y. Han, N. Trainor, S. Kumari, T. V. Knight, J. M. Redwing, Y. Yang and S. Das, *Nature*, 2024, **625**, 276–281.
9. L. Liu, C. Liu, L. Jiang, J. Li, Y. Ding, S. Wang, Y.-G. Jiang, Y.-B. Sun, J. Wang, S. Chen, D. W. Zhang and P. Zhou, *Nat. Nanotechnol.*, 2021, **16**, 874–881.
10. G. Migliato Marega, Y. Zhao, A. Avsar, Z. Wang, M. Tripathi, A. Radenovic and A. Kis, *Nature*, 2020, **587**, 72–77.
11. R. Maiti, C. Patil, M. A. S. R. Saadi, T. Xie, J. G. Azadani, B. Uluutku, R. Amin, A. F. Briggs, M. Miscuglio, D. Van Thourhout, S. D. Solares, T. Low, R. Agarwal, S. R. Bank and V. J. Sorger, *Nat. Photonics*, 2020, **14**, 578–584.
12. S. M. Koepfli, M. Baumann, Y. Koyaz, R. Gadola, A. Güngör, K. Keller, Y. Horst, S. Nashashibi, R. Schwanninger, M. Doderer, E. Passerini, Y. Fedoryshyn and J. Leuthold, *Science*, 2023, **380**, 1169–1174.
13. S. Hwangbo, L. Hu, A. T. Hoang, J. Y. Choi and J.-H. Ahn, *Nat. Nanotechnol.*, 2022, **17**, 500-506.
14. S. Fan, X. Tang, D. Zhang, X. Hu, J. Liu, L. Yang and J. Su, *Nanoscale*, 2019, **11**, 15359–15366.
15. Y. Zhang, P.-A. Chen, Z. Lu, Y. Liu, H. Wei, J. Xia, J. Ding, Z. Gong, C. Peng, W. Shi, Y. Liu, L. Liao and Y. Hu, *Nano Lett.*, 2025, **25**, 3265–3272.
16. S.-Y. Seo, G. Moon, O. F. N. Okello, M. Y. Park, C. Han, S. Cha, H. Choi, H. W. Yeom, S.-Y. Choi, J. Park and M.-H. Jo, *Nat. Electron.*, 2021, **4**, 38-44.
17. J. Jang, J.-K. Kim, J. Shin, J. Kim, K.-Y. Baek, J. Park, S. Park, Y. D. Kim, S. S. P. Parkin, K. Kang, K. Cho and T. Lee, *Sci. Adv.*, 2022, **8**, eabn3181.
18. D. Lee, J. J. Lee, Y. S. Kim, Y. H. Kim, J. C. Kim, W. Huh, J. Lee, S. Park, H. Y. Jeong, Y. D. Kim and C. H. Lee, *Nat. Electron.*, 2021, **4**, 664-670.
19. R. Peng, Y. Wu, B. Wang, R. Shi, L. Xu, T. Pan, J. Guo, B. Zhao, C. Song, Z. Fan, C. Wang, P. Zhou, S. Fan and K. Liu, *Nat. Electron.*, 2023, **6**, 852-861.
20. R. Yang, L. Mei, Z. Lin, Y. Fan, J. Lim, J. Guo, Y. Liu, H. S. Shin, D. Voiry, Q. Lu, J. Li and Z. Zeng, *Nat. Rev. Chem.*, 2024, **8**, 410–432.

21. Y. Gong, H. Yuan, C.-L. Wu, P. Tang, S.-Z. Yang, A. Yang, G. Li, B. Liu, J. van de Groep, M. L. Brongersma, M. F. Chisholm, S.-C. Zhang, W. Zhou and Y. Cui, *Nat. Nanotechnol.*, 2018, **13**, 294–299.
22. Y. Pan, T. Jian, P. Gu, Y. Song, Q. Wang, B. Han, Y. Ran, Z. Pan, Y. Li, W. Xu, P. Gao, C. Zhang, J. He, X. Xu and Y. Ye, *Nat. Commun.*, 2024, 15, 9631.
23. H. Gao, J. Suh, M. C. Cao, A. Y. Joe, F. Mujid, K.-H. Lee, S. Xie, P. Poddar, J.-U. Lee, K. Kang, P. Kim, D. A. Muller and J. Park, *Nano Lett.*, 2020, **20**, 4095-4101.
24. B. Gao, Y. Yan, S. Zhang, Z. Wu, Y. Meng, Y. Zhang, W. Wang, Y. Shen, S. Hu, B. Li, H. Shao, P. Xie, S. P. Yip and J. C. Ho, *Adv. Funct. Mater.*, 2025, **35**, 2425884.
25. J. Zou, Z. Cai, Y. Lai, J. Tan, R. Zhang, S. Feng, G. Wang, J. Lin, B. Liu and H.-M. Cheng, *ACS Nano*, 2021, **15**, 7340-7347.
26. M. Li, X. Wu, W. Guo, Y. Liu, C. Xiao, T. Ou, Y. Zheng and Y. Wang, *J. Mater. Chem. C*, 2022, **10**, 7662-7673.
27. K. Zhang, B. M. Bersch, J. Joshi, R. Addou, C. R. Cormier, C. Zhang, K. Xu, N. C. Briggs, K. Wang, S. Subramanian, K. Cho, S. Fullerton-Shirey, R. M. Wallace, P. M. Vora and J. A. Robinson, *Adv. Funct. Mater.*, 2018, **28**, 1706950.
28. M. Das, D. Sen, N. U. Sakib, H. Ravichandran, Y. Sun, Z. Zhang, S. Ghosh, P. Venkatram, S. Radhakrishnan, A. Sredenschek, Z. Yu, K. J. Sarkar, M. U. K. Sadaf, K. Meganathan, A. Pannone, Y. Han, D. E. Sanchez, D. Somvanshi, Z. Sofer, M. Terrones, Y. Yang and S. Das, *Nat. Electron.*, 2025, **8**, 24–35.
29. H.-P. Komsa and A. V. Krasheninnikov, *Phys. Rev. B*, 2015, **91**, 125304.
30. J.-Y. Noh, H. Kim and Y.-S. Kim, *Phys. Rev. B*, 2014, **89**, 205417.
31. W. Zhou, X. Zou, S. Najmaei, Z. Liu, Y. Shi, J. Kong, J. Lou, P. M. Ajayan, B. I. Yakobson and J.-C. Idrobo, *Nano Lett.*, 2013, **13**, 2615–2622.
32. Y. Zhang, G. Zhu and J. Yang, *Nanoscale*, 2023, **15**, 12116-12122.
33. M. Tosun, L. Chan, M. Amani, T. Roy, G. H. Ahn, P. Taheri, C. Carraro, J. W. Ager, R. Maboudian and A. Javey, *ACS Nano*, 2016, **10**, 6853-6860
34. P.-C. Shen, Y. Lin, C. Su, C. McGahan, A.-Y. Lu, X. Ji, X. Wang, H. Wang, Nannan Mao, Y. Guo, J.-H. Park, Y. Wang, W. Tisdale, J. Li, Xi Ling, K. E. Aidala, T. Palacios and J. Kong, *Nat. Electron.*, 2022, **5**, 28–36
35. Y. Jeong, B. Han, A. Tamayo, N. Claes, S. Bals and P. Samorì, *ACS Nano*, 2024, **18**, 18334–18343
36. H. Im, A. Bala, B. So, Y. J. Kim and S. Kim, *Adv. Electron. Mater.*, 2021, **7**, 2100644.
37. Y. Guo, J. Li, X. Zhan, C. Wang, M. Li, B. Zhang, Z. Wang, Y. Liu, K. Yang, H. Wang, W. Li, P. Gu, Z. Luo, Y. Liu, P. Liu, B. Chen, K. Watanabe, T. Taniguchi, X. Q. Chen, C. Qin, J. Chen, D. Sun, J. Zhang, R. Wang, J. Liu, Y. Ye, X. Li, Y. Hou, W. Zhou, H. Wang and Z. Han, *Nature*, 2024, **630**, 346-352.
38. N. Onofrio, D. Guzman and A. Strachan, *J. Appl. Phys.*, 2017, **122**, 185102.
39. Y. C. Lin, R. Torsi, D. B. Geohegan and J. A. Robinson, *Adv. Sci.*, 2021, **8**, 2004249
40. L. Tang, R. Xu, J. Tan, Y. Luo, J. Zou, Z. Zhang, R. Zhang, Y. Zhao, J. Lin, X. Zou, B. Liu and H.-M. Cheng, *Adv. Funct. Mater.*, 2020, **31**, 2006941.
41. R. Torsi, K. T. Munson, R. Pendurthi, E. A. Marques, B. Van Troeye, L. Huberich, B. Schuler, M. A. Feidler, K. Wang, G. Pourtois, S. Das, J. B. Asbury, Y.-C. Lin and J. A. Robinson, *ACS Nano*, 2023, **17**, 15629-15640.

42. B. Gao, W. Wang, Y. Meng, C. Du, Y. Long, Y. Zhang, H. Shao, W. Wang, P. Xie, S. P. Yip, X. Zhong and J. C. Ho, *Small*, 2024, **20**, 2402217.
43. V. T. Vu, T. T. H. Vu, T. L. Phan, W. T. Kang, Y. R. Kim, M. D. Tran, H. T. T. Nguyen, Y. H. Lee and W. J. Yu, *ACS Nano*, 2021, **15**, 13031–13040.
44. J. Jiang, L. Xu, L. Du, L. Li, G. Zhang, C. Qiu and L.-M. Peng, *Nat. Electron.*, 2024, **7**, 545–556
45. Z. Wang, M. Tripathi, Z. Golsanamlou, P. Kumari, G. Lovarelli, F. Mazziotti, D. Logoteta, G. Fiori, L. Sementa, G. Migliato Marega, H. G. Ji, Y. Zhao, A. Radenović, G. Iannaccone and A. Kis, *Adv. Mater.*, 2023, **35**, 2209371
46. K. Ko, M. Jang, J. Kwon and J. Suh, *J. Appl. Phys.*, 2024, **135**, 100901.
47. M. Suleman, S. Lee, M. Kim, M. Riaz, Z. Abbas, H. M. Park, V. H. Nguyen, N. Nasir, S. Kumar, J. Jung and Y. Seo, *Mater. Today Phys.*, 2024, **43**, 101427.
48. F. Zhong, J. Ye, T. He, L. Zhang, Z. Wang, Q. Li, B. Han, P. Wang, P. Wu, Y. Yu, J. Guo, Z. Zhang, M. Peng, T. Xu, X. Ge, Y. Wang, H. Wang and W. Hu, *Small*, 2021, **17**, 2102855.
49. S. Wi, H. Kim, M. Chen, H. Nam, L. J. Guo, E. Meyhofer and X. Liang, *ACS Nano*, 2014, **8**, 5270–5281.
50. J. Lu, Z. Guo, W. Wang, J. Lu, Y. Hu, J. Wang, Y. Xiao, X. Wang, S. Wang, Y. Zhou and X. Zeng, *Nanotechnology*, 2021, **32**, 015701.
51. Y. Kang, Y. Pei, D. He, H. Xu, M. Ma, J. Yan, C. Jiang, W. Li and X. Xiao, *Light: Sci. Appl.*, 2024, **13**, 127.
52. S. Ullah, L. Li, Y. Wang, X. Yang, M. Tang, Y. Xiang and Q. Yang, *J. Mater. Chem. C*, 2023, **11**, 3386–3394.
53. S. G. Seo, J. Jeong, S. Y. Kim, A. Kumar and S. H. Jin, *Nano Res.*, 2021, **14**, 3214–3227.
54. Y. Chen, R. Wang, D. Li, Q. Huang, Y. Tang, H. Ren, Y. Wang, G. Liu, F. Li, H. Wang and B. Zhu, *Small*, 2025, **21**, 2503836.
55. W. Deng, Y. Yu, X. Yan, L. Wang, N. Yu, X. Liao, W. Luo and J. Wu, *ACS Nano*, 2025, **19**, 27526–27537.
56. S. Bhattacharjee, R. Wigchering, H. G. Manning, J. J. Boland and P. K. Hurley, *Sci. Rep.*, 2020, **10**, 12178.
57. L. Li, W. Dang, X. Zhu, H. Lan, Y. Ding, Z.-A. Li, L. Wang, Y. Yang, L. Fu, F. Miao and M. Zeng, *Adv. Mater.*, 2025, **37**, e2309296
58. A. Söll, E. Lopriore, A. K. Ottesen, J. Luxa, G. Pasquale, J. Sturala, F. Hájek, V. Jarý, D. Sedmidubský, K. Mosina, I. Sokolović, S. Rasouli, T. Grasser, U. Diebold, A. Kis and Z. Sofer, *ACS Nano*, 2024, **18**, 10397–10406.
59. H. Agarwal, B. Terrors, L. Orsini, A. Montanaro, V. Sorianello, M. Pantouvaki, K. Watanabe, T. Taniguchi, D. Van Thourhout, M. Romagnoli and F. H. L. Koppens, *Nat. Commun.*, 2021, **12**, 20926.
60. Z. Lu, Y. Chen, W. Dang, L. Kong, Q. Tao, L. Ma, D. Lu, L. Liu, W. Li, Z. Li, X. Liu, Y. Wang, X. Duan, L. Liao and Y. Liu, *Nat. Commun.*, 2023, **14**, 2340.
61. T. Sohier, D. Campi, N. Marzari and M. Gibertini, *Phys. Rev. Mater.*, 2018, **2**, 114010.
62. T. Ando, A. B. Fowler and F. Stern, *Rev. Mod. Phys.*, 1982, **54**, 437–672.
63. P. Cudazzo, I. V. Tokatly and A. Rubio, *Phys. Rev. B*, 2011, **84**, 085406.

View Article Online
DOI: 10.1039/D5NR05242D

64. S. V. Suryavanshi and E. Pop, *J. Appl. Phys.*, 2016, **120**, 224503
65. T. Knobloch, B. Uzlu, Y. Y. Illarionov, Z. Wang, M. Otto, L. Filipovic, M. Waltl, D. Neumaier, M. C. Lemme and T. Grasser, *Nat. Electron.*, 2022, **5**, 356–366.
66. Z. Bian, J. Miao, T. Zhang, H. Chen, Q. Zhu, J. Chai, F. Tian, S. Wu, Y. Xu, B. Yu, Y. Chai and Y. Zhao, *Small*, 2023, **19**, e2206791.
67. K. Ko, J. Huang, J. Kwon, M. Jang, H. Cho, S. Yang, S. Kim, S. Park, T. Taniguchi, K. Watanabe, D. Y. Lin, S. Singh, D. H. Lim, S. A. Tongay, J. Kang and J. Suh, *ACS Nano*, 2025, **19**, 1630–1641.
68. A. Laturia, M. L. Van de Put and W. G. Vandenberghe, *npj 2D Mater. Appl.*, 2018, **2**, 6.
69. Y. Liu, P. Stradins and S.-H. Wei, *Sci. Adv.*, 2016, **2**, e1600069
70. G. Kwon, H.-S. Kim, J. Hwang, S. Lee, S. Oh … *Nat. Electron.*, 2022, **5**, 241–247
71. J. Zhang, A. Yang, X. Wu, J. van de Groep, P. Tang, S. Li, B. Liu, F. Shi, J. Wan, Q. Li, Y. Sun, Z. Lu, X. Zheng, G. Zhou, C. L. Wu, S.-C. Zhang, M. L. Brongersma, J. Li and Y. Cui, *Nat. Commun.*, 2018, **9**, 5289.
72. J. Kwon, H. Cho, K. Ko, H. Kim, S. Yang, J. Yeo, K. H. Lee, H.-H. Cho and J. Suh, *Nano Lett.*, 2025, **25**, 12585–12592.
73. K. Matsuyama, R. Aoki, K. Miura, A. Fukui, Y. Togawa, T. Yoshimura, N. Fujimura and D. Kiriya, *ACS Appl. Mater. Interfaces*, 2022, **14**, 8163–8170.
74. L. Zhang, Z. Wang, Z. Zhang, J. Chen, B. Liang, X. Quan, Y. Dai, J. Huang, Y. Wang, S.-J. Long, M. Si, F. Miao, Y. Peng, Y. Zhang and J. Li, *Adv. Funct. Mater.*, 2022, **32**, 2204760.
75. Y. S. Jung, J. Y. Kim, W. Shen, S. Y. Han, H. Kim and Y. S. Cho, *ACS Nano*, 2025, **19**, 17438–17449.
76. B. Zheng, X. Sun, W. Zheng, C. Zhu, C. Ma, A. Pan, D. Li and S. Li, *Front. Optoelectron.*, 2023, **16**, 42
77. R. Tomar, B. Hsu, A. Perez, M. Stroscio and M. Dutta, *J. Electron. Mater.*, 2023, **52**, 5513–5520.
78. J. Hong, Z. Hu, M. Probert, K. Li, D. Lv, X. Yang, L. Gu, N. Mao, Q. Feng, L. Xie, J. Zhang, D. Wu, Z. Zhang, C. Jin, W. Ji, X. Zhang, J. Yuan and Z. Zhang, *Nat. Commun.*, 2015, **6**, 6293.
79. X. Zhang, J. Xu, A. Zhi, J. Wang, Y. Wang, W. Zhu, X. Han, X. Tian, X. Bai, B. Sun, Z. Wei, J. Zhang and K. Wang, *Adv. Sci.*, 2024, **11**, e2408640.
80. J. Suh, T. L. Tan, W. Zhao, J. Park, D.-Y. Lin, T.-E. Park, J. Kim, C. Jin, N. Saigal, S. Ghosh, Z. M. Wong, Y. Chen, F. Wang, W. Walukiewicz, G. Eda and J. Wu, *Nat. Commun.*, 2018, **9**, 199.
81. Z. Qin, L. Loh, J. Wang, X. Xu, Q. Zhang, B. Haas, C. Alvarez, H. Okuno, J. Zhou Yong, T. Schultz, N. Koch, J. Dan, S. J. Pennycook, D. Zeng, M. Bosman and G. Eda, *ACS Nano*, 2019, **13**, 10768–10775.
82. L. Loh, Y. W. Ho, F. Xuan, A. del Águila, Y. Chen, S. Y. Wong, J. Zhang, Z. Wang, K. Watanabe, T. Taniguchi, P. Pigram, M. Bosman, S. Y. Quek and G. Eda, *Nat. Commun.*, 2024, **15**, 10035.
83. H. G. Ji, P. Solís-Fernández, D. Yoshimura, M. Maruyama, T. Endo, Y. Miyata, S. Okada and H. Ago, *Adv. Mater.*, 2019, **31**, 1903613.

84. P. Zhang, N. Cheng, M. Li, B. Zhou, C. Bian, Y. Wei, X. Wang, H. Jiang, L. Bao, Y. Lin, Z. Hu, Y. Du and Y. Gong, *ACS Appl. Mater. Interfaces*, 2020, **12**, 18650–18659.
85. Y. S. Shin, K. Lee, D. D. Loc, J. S. Kim, W. T. Kang, J. E. Kim, U. Y. Won, I. Lee, H. Lee, J. Heo, S. Park, Y. H. Lee and W. J. Yu, *Adv. Funct. Mater.*, 2020, **30**, 2003688.
86. K. Zhang, D. D. Deng, B. Zheng, Y. Wang, F. K. Perkins, N. C. Briggs, V. H. Crespi and J. A. Robinson, *Adv. Mater. Interfaces*, 2020, **7**, 2000856.
87. Li Yang, H. Wu, G. Zhang, W. Jin, L. Li, W. Zhang and H. Chang, *Cell Rep. Phys. Sci.*, 2022, **3**, 100953.
88. A. Kozhakhmetov, B. Schuler, A. M. Z. Tan, K. A. Cochrane, J. R. Nasr, H. El-Sherif, A. Bansal, A. Vera, V. Bojan, J. M. Redwing, N. Bassim, S. Das, R. G. Hennig, A. Weber-Bargioni and J. A. Robinson, *Adv. Mater.*, 2020, **32**, e2005159.
89. V. T. Vu, T. L. Phan, T. T. H. Vu, M. H. Park, V. D. Do, V. Q. Bui, K. Kim, Y. H. Lee and W. J. Yu, *ACS Nano*, 2022, **16**, 12073–12082.
90. M. M. Ugeda, A. J. Bradley, S.-F. Shi, F. H. da Jornada, Y. Zhang, D. Y. Qiu, W. Ruan, S.-K. Mo, Z. Hussain, Z.-X. Shen, F. Wang, S. G. Louie and M. F. Crommie, *Nat. Mater.,* 2014, **13**, 1091–1095.
91. H.-P. Komsa and A. V. Krasheninnikov, *Phys. Rev. B*, 2012, **86**, 241201.
92. T. Y. Jeong, H. Kim, S.-J. Choi, K. Watanabe, T. Taniguchi, K. J. Yee, Y.-S. Kim and S. Jung, *Nat. Commun.,* 2019, **10**, 3825.
93. S.-C. Lu and J.-P. Leburton, *Nanoscale Res. Lett.,* 2014, **9**, 676.
94. S. Chowdhury, P. Venkateswaran and D. Somvanshi, *Europhys. Lett.,* 2022, **137**, 26004.
95. J. Zhou, J. Lin, H. Sims, C. Jiang, C. Cong, J. A. Brehm, Z. Zhang, L. Niu, Y. Chen, Y. Zhou, Y. Wang, F. Liu, C. Zhu, T. Yu, K. Suenaga, R. Mishra, S. T. Pantelides, Z.-G. Zhu, W. Gao, Z. Liu and W. Zhou, *Adv. Mater*., 2020, **32**, 1906536.
96. S. Fu, K. Kang, K. Shayan, A. Yoshimura, S. Dadras, X. Wang, L. Zhang, S. Chen, N. Liu, A. Jindal, X. Li, A. N. Pasupathy, A. N. Vamivakas, V. Meunier, S. Strauf and E.-H. Yang, *Nat. Commun.*, 2020, **11**, 2034.
97. E. Liu, Y. Fu, Y. Wang, Y. Feng, H. Liu, X. Wan, W. Zhou, B. Wang, L. Shao, C.-H. Ho, Y.-S. Huang, Z. Cao, L. Wang, A. Li, J. Zeng, F. Song, X. Wang, Y. Shi, H. Yuan, H. Y. Hwang, Y. Cui, F. Miao and D. Xing, *Nat. Commun.,* 2015, **6**, 6991.
98. Y.-C. Lin, H.-P. Komsa, C.-H. Yeh, T. Björkman, Z.-Y. Liang, C.-H. Ho, Y.-S. Huang, P.-W. Chiu, A. V. Krasheninnikov and K. Suenaga, *ACS Nano*, 2015, **9**, 11249-11257.

View Article Online
DOI: 10.1039/D5NR05242D

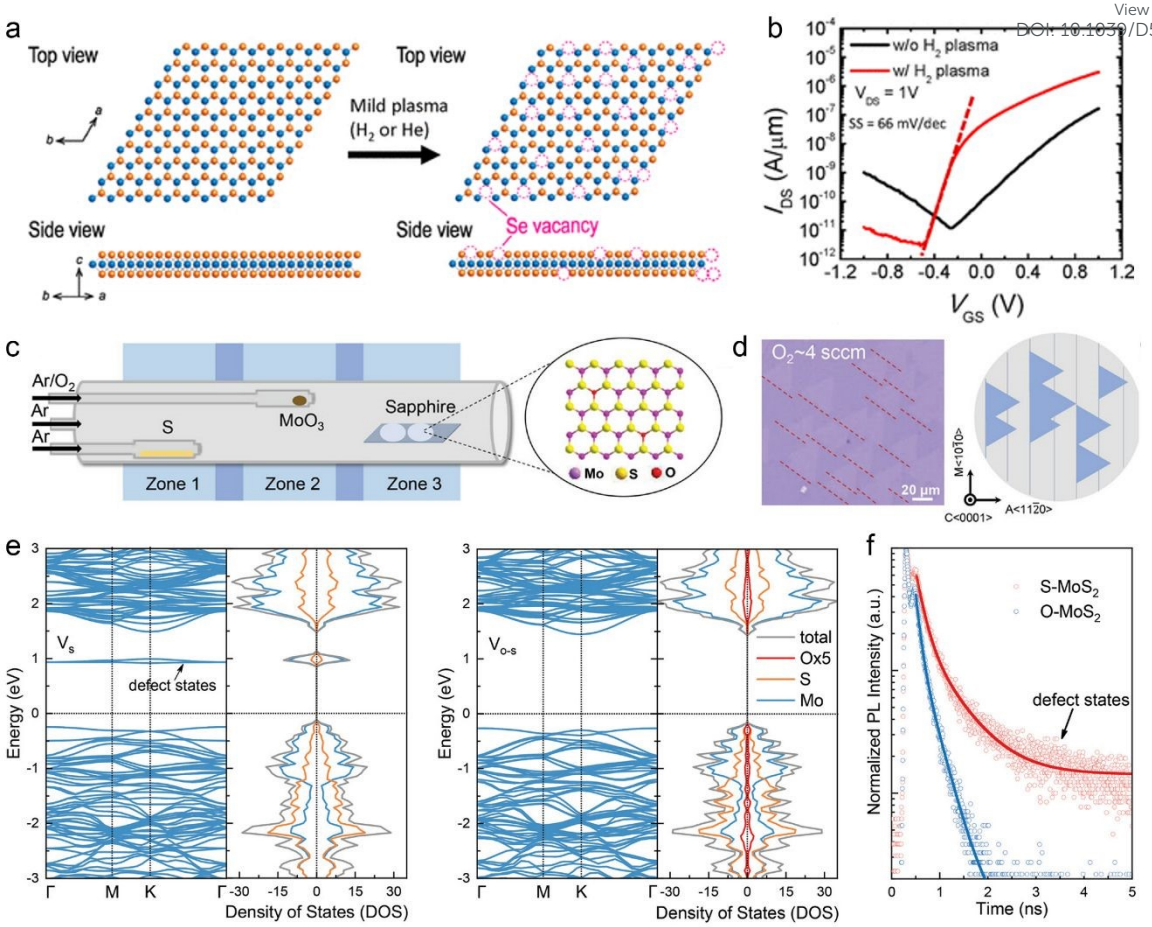

Fig. 1 | Defect engineering strategies for carrier-polarity control in 2D TMDs.
(a) Schematic illustration of mild H_2 or He plasma exposure on monolayer WSe_2, leading to controlled creation of Se vacancies at the topmost layer. (b) Transfer-characteristics curves of WSe_2 FETs showing that plasma-induced Se vacancies enhance *n*-type conduction and yield a negative threshold-voltage shift compared with pristine devices. (c) Schematic of an O_2-assisted CVD setup for oxygen-incorporated MoS_2 growth, where oxygen atoms substitute sulfur vacancies to form Mo–O bonds. (d) Optical micrograph and domain-orientation mapping of oxygen-incorporated MoS_2 films grown at $O_2 \approx 4$ sccm, (e) Calculated electronic band structures and densities of states showing elimination of vacancy-derived mid-gap defect levels after O substitution. (f) Time-resolved photoluminescence spectra demonstrating prolonged carrier lifetimes in O-doped MoS_2 owing to defect-state suppression, confirming uniform triangular grains on sapphire. Reproduced from Ref. [33] (panels a,b) and Ref. [79] (panels c–f) with permission under the Creative Commons Attribution License (CC BY 4.0).

View Article Online
DOI: 10.1039/D5NR05242D

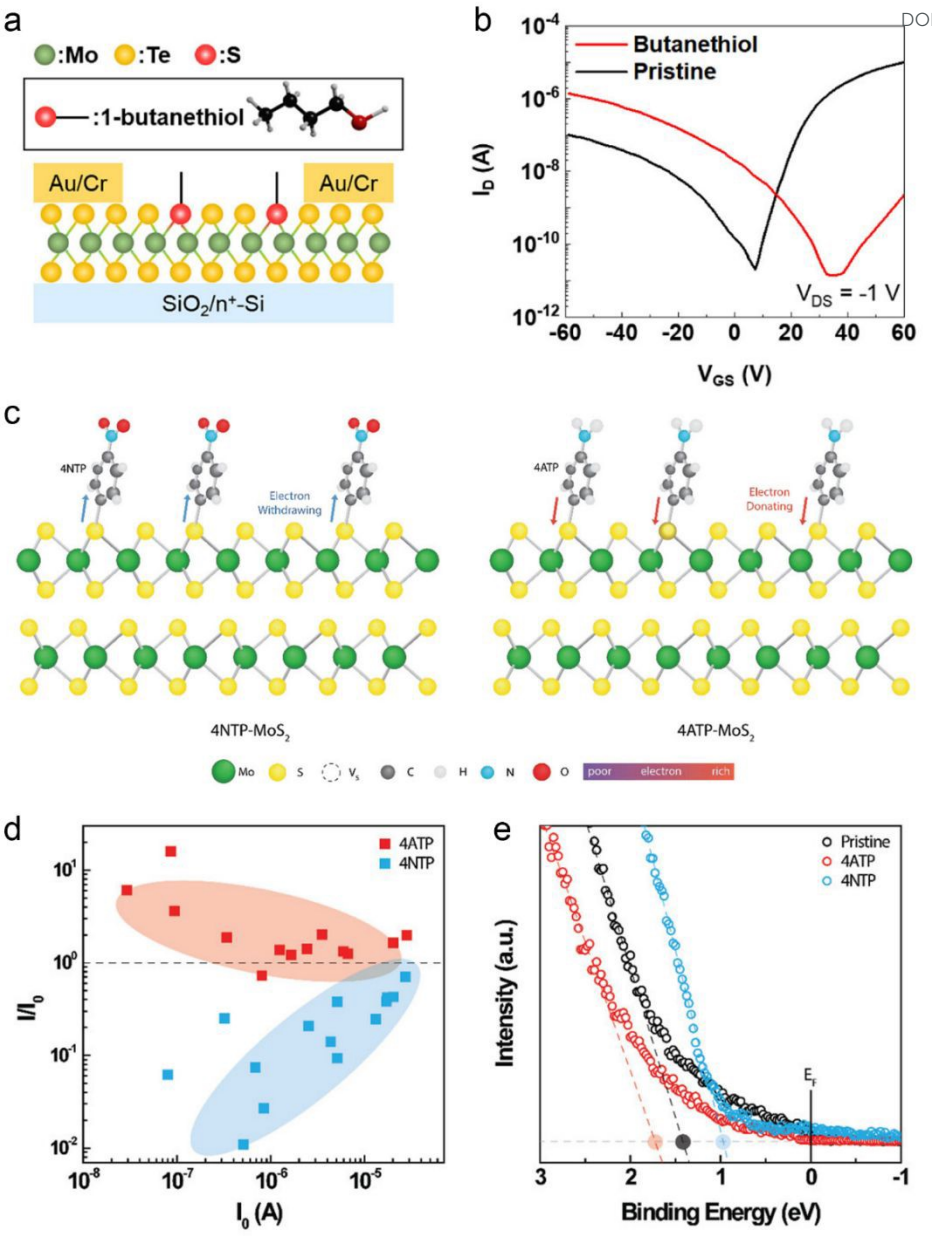

Fig. 2 | Surface charge-transfer mechanisms for molecular doping of 2D TMDs.
(a) Schematic illustration of 1-butanethiol molecular adsorption on monolayer $MoTe_2$, forming surface dipoles that withdraw electrons from the channel. (b) Transfer characteristics of $MoTe_2$ FETs before and after butanethiol functionalization, showing a positive V_{th} shift and enhanced *p*-type conduction. (c) Schematic models of 4-aminothiophenol (4ATP, electron-donating) and 4-nitrothiophenol (4NTP, electron-withdrawing) adsorption on MoS_2, illustrating opposite charge-transfer directions. (d) Statistical I_{on}/I_{off} ratios comparison demonstrating *p*-type conversion with 4ATP and *n*-type reinforcement with 4NTP. (e) Ultraviolet photoelectron spectra (UPS) confirming Fermi-level upshift (4NTP) and downshift (4ATP) via interfacial dipole modulation. Reproduced from Ref. [35] (panels a,b) and Ref. [36] (panels c–e) under the Creative Commons Attribution License (CC BY 4.0).

View Article Online
DOI: 10.1039/D5NR05242D

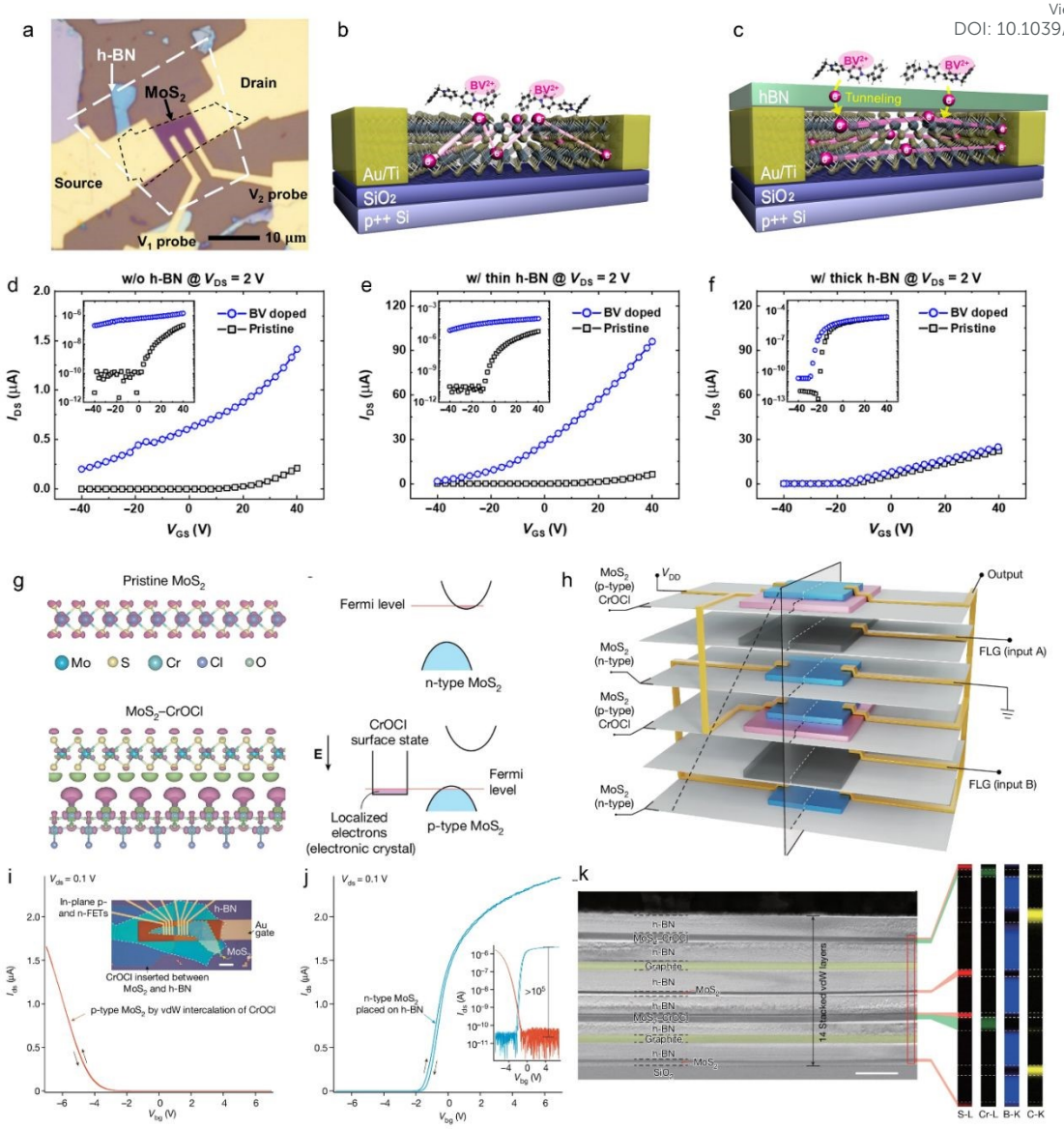

Fig. 3 | Remote charge-transfer modulation of 2D TMDs through vdW heterointerfaces. (a) Optical micrograph of MoS_2 device partially covered with h-BN for non-contact charge-transfer measurement. (b) Schematic of benzyl viologen (BV) molecular adsorption directly on MoS_2 surface producing electron donation and *n*-type enhancement. (c) Introduction of h-BN spacer layer enabling remote electron tunneling from BV through vdW gap. (d–f) Transfer curves comparing BV-doped and pristine MoS_2 under different h-BN thicknesses, highlighting gradual suppression of direct charge transfer and tunable electron injection. (g) Atomistic model and band-alignment schematic of MoS_2/CrOCl heterostructure illustrating remote hole transfer from CrOCl surface states to MoS_2. (h) Conceptual diagram of stacked MoS_2/CrOCl heterostructure integrated for complementary logic operation. (i,j) Transfer curves of *p*-type MoS_2 (CrOCl coupled) and *n*-type MoS_2 controls showing clear bipolar behavior. (k) Cross-sectional STEM image of the heterostack confirming clean vdW interfaces. Reproduced from Ref. [17] (panels a–f) and Ref. [37] (panels g–k) under the Creative Commons Attribution License (CC BY 4.0).

View Article Online
DOI: 10.1039/D5NR05242D

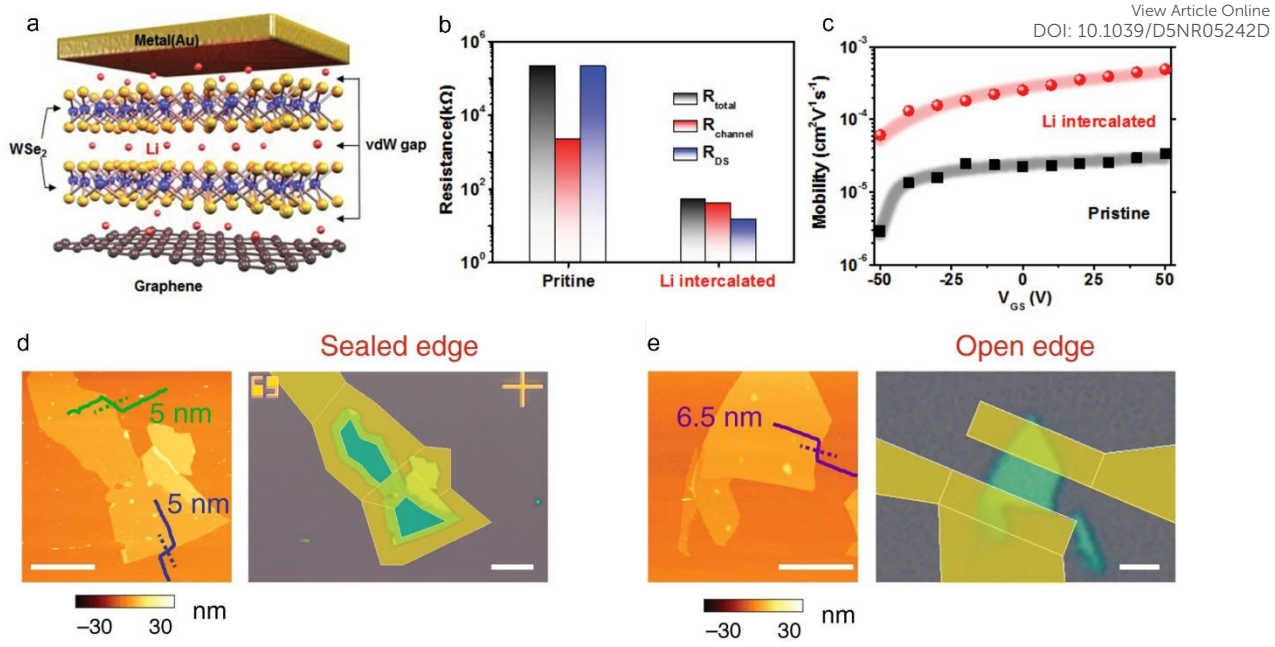

Fig. 4 | Intercalation-driven carrier and interface modulation in vdW semiconductors. (a) Schematic illustration of Li^+ intercalation into WSe_2 vdW gaps forming Au/WSe_2/graphene vertical junctions. (b) Comparison of total, channel, and contact resistances before and after Li insertion, showing a Schottky-to-ohmic transition. (c) Field-effect mobility enhancement after Li intercalation attributed to flattened electrostatic potential and reduced interlayer resistance. (d) AFM and optical micrographs of few-layer MoS_2 flakes with sealed edges after ion intercalation, preserving lattice integrity. (e) Corresponding images of open-edge MoS_2 regions enabling rapid ion diffusion and full 2H→1T′ phase transformation. Reproduced from Ref. [85] (panels a–c) and Ref. [71] (panels d-e) under the Creative Commons Attribution License (CC BY 4.0).

View Article Online
DOI: 10.1039/D5NR05242D

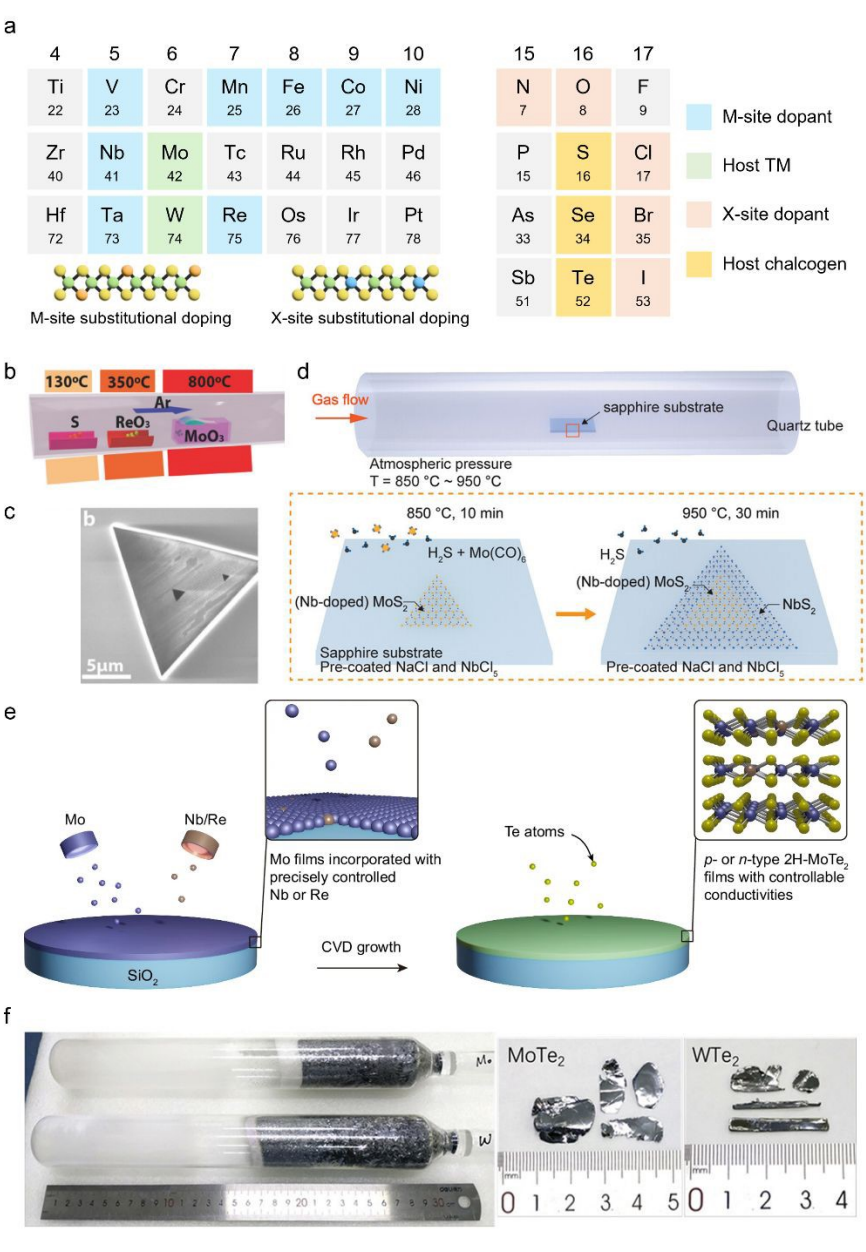

Fig. 5 | Substitutional doping in TMDs with various dopant candidates and synthesis route.

(a) Schematic illustration of substitutional doping at the metal (M) and chalcogen (X) sites. The periodic table highlights available dopants for M-sites (light blue) and X-sites (orange) relative to host transition metals (green) and chalcogens (yellow). (b,c) Stepwise temperature-controlled chemical vapor deposition growth of Re-doped MoS_2, showing precursor arrangement and triangular flake morphology with Re incorporation. (d) Atmospheric-pressure MOCVD process for Nb-doped MoS_2 using NaCl seeding and $NbCl_5$ vapor transport, illustrating multi-zone temperature control and gas-phase reaction sequence. (e) Co-sputtering–assisted CVD approach for Nb and Re incorporation in $MoTe_2$, forming *p*- or *n*-type 2H-$MoTe_2$ films with controllable conductivity. (f) CVT-grown bulk $MoTe_2$ and WTe_2 single crystals with dopant incorporation for high-purity wafer-scale counter-doped crystals. Reproduced from Ref. [27] (panels b.c), Ref. [45] (panel d), Ref. [22] (panel e), and Ref. [87] (panel f) under the

View Article Online
DOI: 10.1039/D5NR05242D

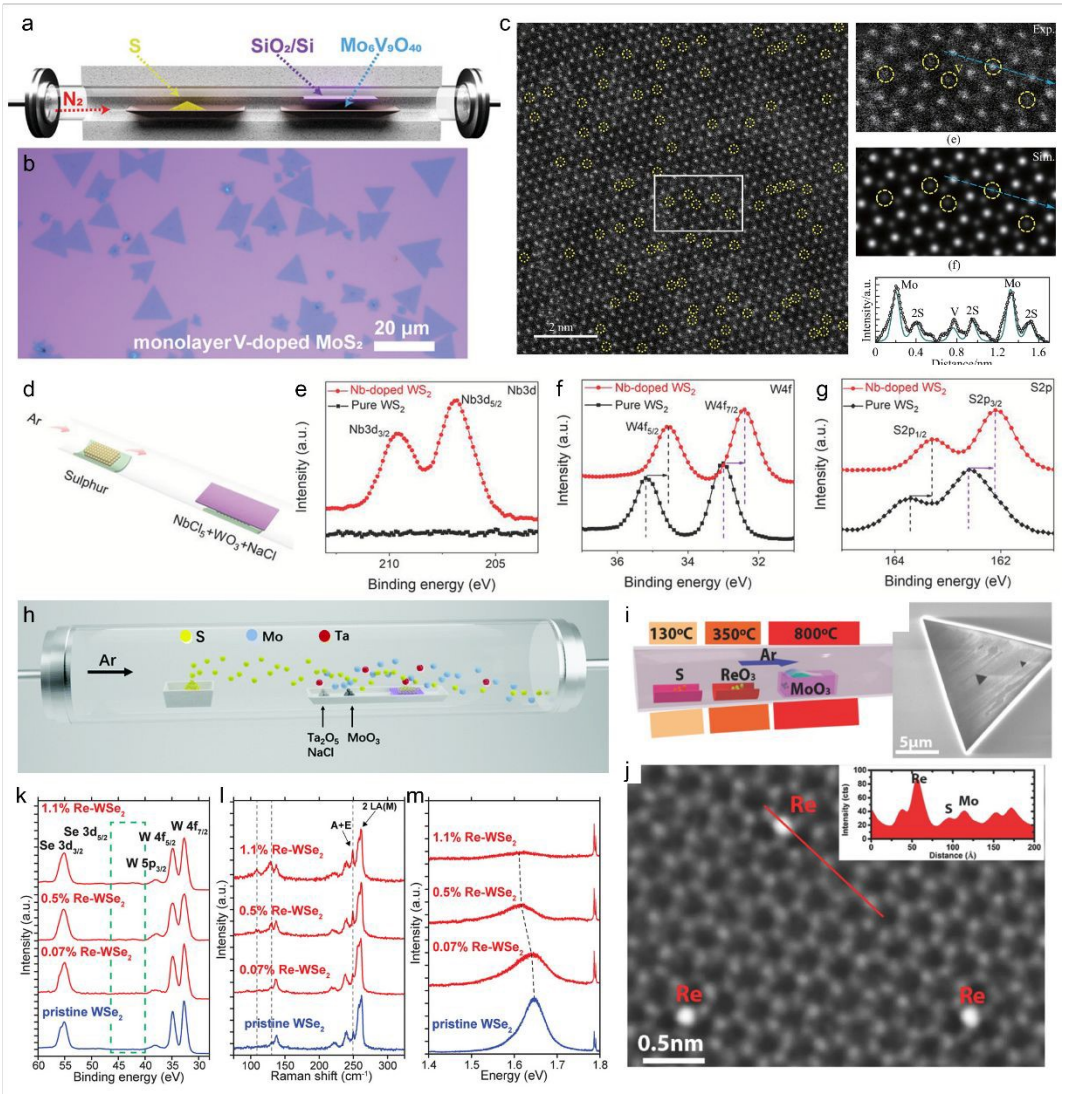

Fig. 6 | Representative substitutional counter-doping across 2D TMDs.
(a) Schematic image in CVD growth of V-doped MoS_2 using mixed oxide precursors (MoO_3–V_2O_5) and S vapor and (b) OM image of as-grown monolayer triangular flakes of V-doped MoS_2 with controlled V incorporation. (c) Atomic-resolution HAADF-STEM image of V-doped MoS_2 highlighting substitutional V atoms at Mo sites and corresponding intensity line profile. (d) One-step Nb substitutional doping of WS_2 through $NbCl_5$ vapor transport and NaCl-assisted CVD, and (e-g) XPS spectra confirming Nb 3d, W 4f, and S 2p core-level shifts indicative of *p*-type behavior. (h) Schematic of Ta-doped MoS_2 synthesis using Ta_2O_5 and NaCl under Ar flow, showing precursor distribution and one-zone CVD configuration. (i) Temperature-controlled in-situ Re incorporation during MoS_2 CVD using ReO_3 and MoO_3, displaying triangular monolayers and (j) atomic-resolution STEM image identifying Re atoms substituting Mo. (k–m) Substitutional Re-doping of WSe_2 via MOCVD, evidenced by XPS (W 4f, S 2p peaks), Raman red-shift, and PL quenching with increasing Re concentration. Reproduced from Ref. [74] (panels a,b); Ref. [76] (panel c); Ref. [40] (panels d-g); Ref. [26] (panel h); Ref. [27] (panel i,j); and Ref. [88] (panels k-m) under Creative Commons license (CC BY).

View Article Online
DOI: 10.1039/D5NR05242D

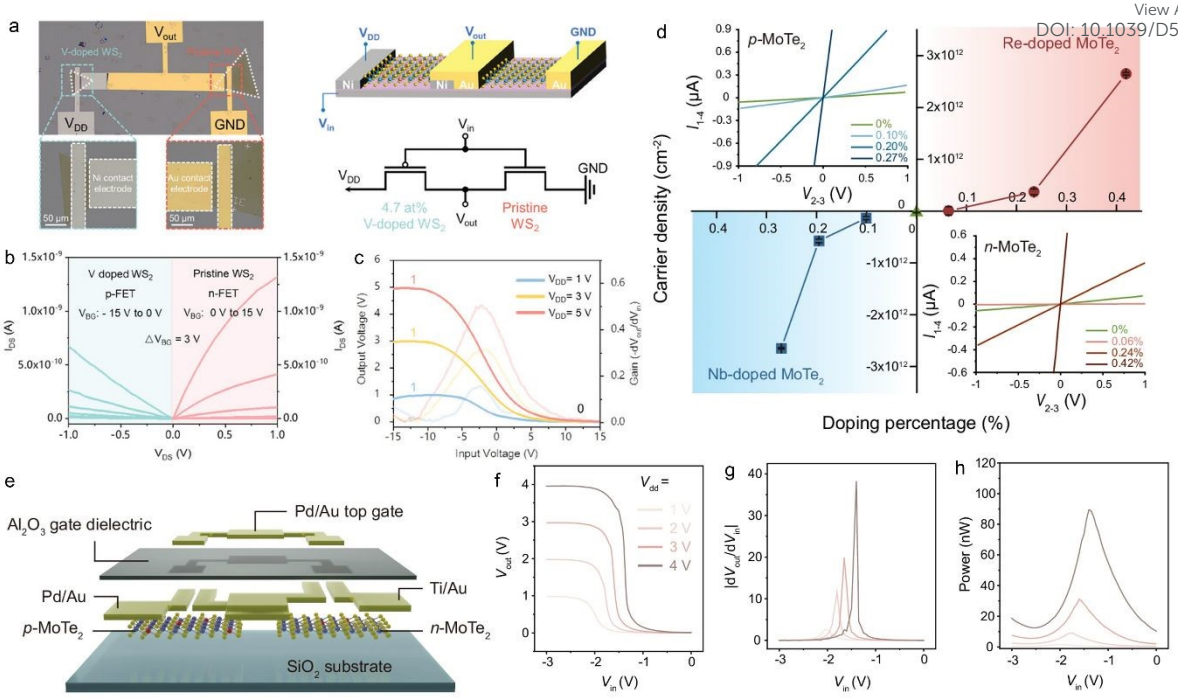

Fig. 7 | Substitutional doping–enabled CMOS inverter demonstrations in 2D TMDs. (a) OM image and schematic illustration of a CMOS inverter constructed from *p*-type 4.7 at% V-doped WS_2 and pristine *n*-type WS_2 monolayers. Ni and Au serve as contact electrodes for *p*- and *n*-FETs, respectively. (b) Output characteristics of V-doped WS_2 *p*-FET and pristine WS_2 *n*-FET showing clear complementary transfer behavior. (c) Voltage-transfer curves and corresponding gains at different supply voltages (V_{DD} = 1,3,5 V), exhibiting stable logic inversion. (d) Carrier-type conversion and doping-dependent transport characteristics of Nb- and Re-doped 2H-$MoTe_2$, showing progressive *p*-type behavior with Nb and *n*-type behavior with Re incorporation, which are extracted by Hall measurements. (e) Device structure of complementary *p*-$MoTe_2$ and *n*-$MoTe_2$ FETs forming monolithic CMOS inverters on SiO_2/Si substrate. (f) Voltage-transfer characteristics, (g) corresponding voltage gains, and (h) static power consumption of the 2D CMOS inverter under different V_{DD} values (1–4 V). Reproduced from Ref. [42] (panels a-c) and Ref. [22] (panels d-h) under Creative Commons license (CC BY).

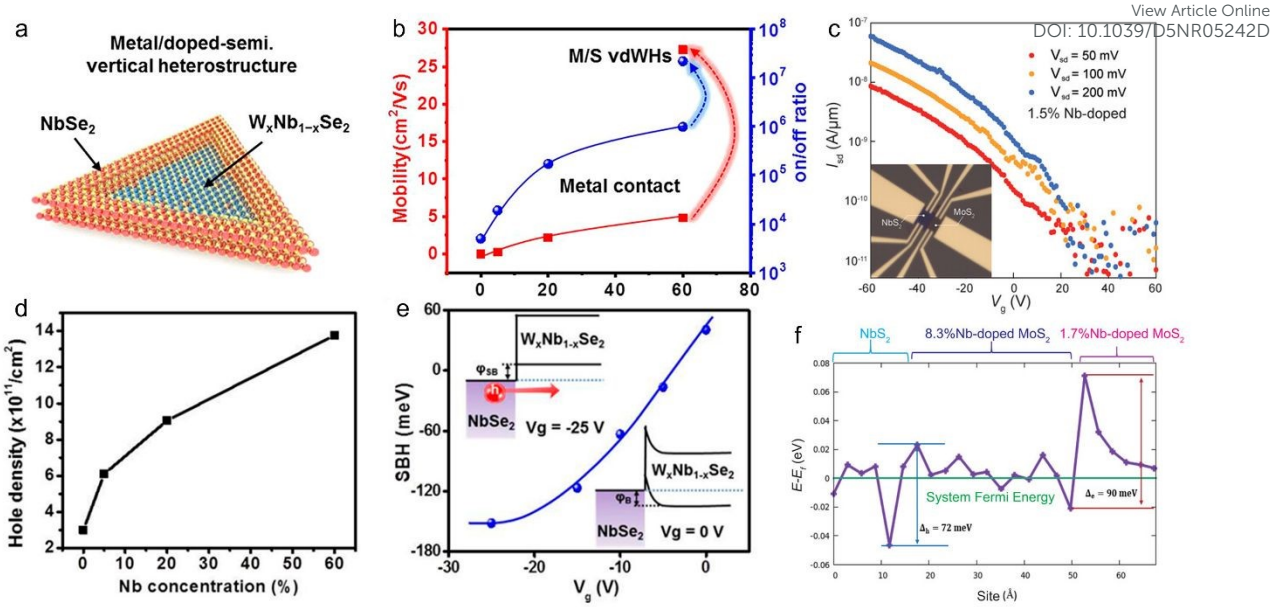

Fig. 8 | Substitutional-doping-assisted ohmic contact engineering in 2D TMDs.
(a) Schematic illustration of $NbSe_2/W_xNb_{1-x}Se_2$ metal/doped-semiconductor heterostructure synthesized by one-step CVD growth. (b) Comparison of field-effect mobility (left axis) and on/off ratio (right axis) between conventional metal-contacted WSe_2 and $NbSe_2/W_xNb_{1-x}Se_2$ van der Waals heterostructures. (c) Transfer characteristics of the NbS_2–MoS_2 lateral heterostructure, confirming stable *p*-type conduction. (Inset: OM image of the device). (d) Variation of hole carrier density in WSe_2 with increasing Nb incorporation (0–60%). (e) Extracted Schottky barrier height (Φ_{SB}) as a function of gate voltage, showing a negative (Φ_{SB}) (≈ −0.68 eV) at the $NbSe_2/W_xNb_{1-x}Se_2$ interface, indicative of *p*-type ohmic contact formation. (f) Calculated planar-averaged electrostatic potential across the NbS_2–MoS_2 interface, revealing a minimal potential step (ΔE ≈ 72–90 meV) that facilitates efficient hole transport. Reproduced from Ref. [43] (panels a,b,d,e) and Ref. [45] (panels c,f) under Creative Commons license (CC BY).

View Article Online
DOI: 10.1039/D5NR05242D

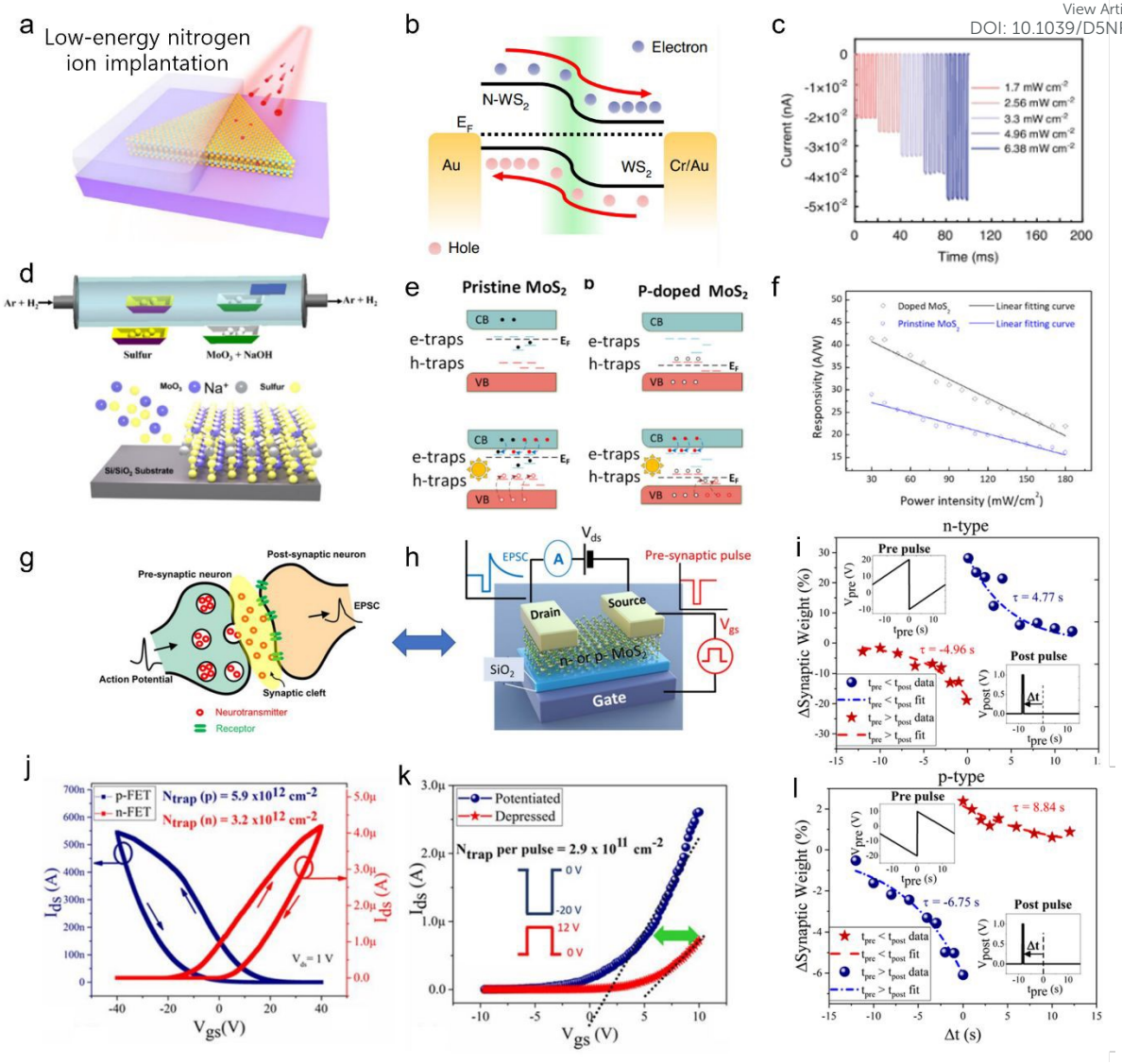

Fig. 9 | Doping-Enabled Optoelectronic and Neuromorphic Devices.
(a) Schematic of nitrogen implantation into monolayer WS_2. (b) Band diagram illustrating carrier separation at the N-WS_2/WS_2 junction. (c) Time-resolved photocurrent under varying optical power, showing rectification and strong photoresponse. (d) Schematic growth process enabling Na intercalation in MoS_2. (e) Band structure of in pristine and *p*-doped MoS_2 under dark and illumination. (f) Power-dependent responsivity. (g) Synaptic response schematic. (h) Measurement scheme showing synaptic emulation based on charge trapping/de-trapping in Re- or Nb-doped MoS_2, with presynaptic gate pulses and EPSC recorded at a constant drain bias. (j) Hysteresis characteristics of Re-doped (*n*-type) and Nb-doped (*p*-type) MoS_2 transistors. (k) Threshold-voltage shift induced by 50 consecutive gate pulses, evidencing cumulative charge-trapping dynamics. (i,l) STDP characteristics for synaptic devices of (i) Re-doped and (l) Nb-doped MoS_2, showing synaptic weight changes (Δ Synaptic Weight%) as a function of the pre–post spike interval (Δt), closely resembling biological synapses. Reproduced from Ref. [51] (panels a-c), Ref. [52] (panels (d-f) and Ref. [56] (panels g-l) under Creative Commons license (CC BY).

View Article Online
DOI: 10.1039/D5NR05242D

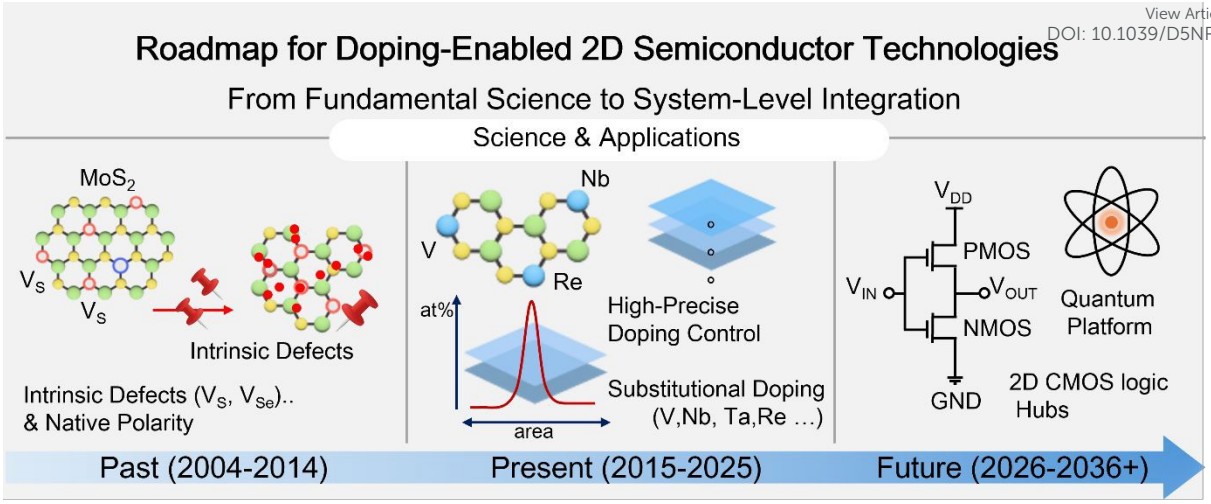

Fig. 10 | Conceptual Roadmap for Doping-Enabled 2D Semiconductor Technologies. Schematic illustration of technological roadmap of doping-enabled 2D semiconductors. (Left) Investigation of intrinsic defects and early-stage defect challenges (2004-2014). (Center) Development of high-precision substitutional doping using various transition metals (2015-2025). (Right) System-level integration toward 2D CMOS logic hubs and quantum platforms (2026-2036+).

Counter-Doping in Two-Dimensional Transition-Metal Dichalcogenides: Flipping Native Polarity and Beyond

View Article Online
DOI: 10.1039/D5NR05242D

Sungyeon Kim[1], Jeongin Yeo[1], Hongsik Jeong[1], Joonki Suh[2,★]

[1] Department of Materials Science and Engineering, Ulsan National Institute of Science and Technology (UNIST), Ulsan 44919, Republic of Korea

[2] Department of Chemical and Biomolecular Engineering, Korea Advanced Institute of Science and Technology (KAIST), 34141 Daejeon, Republic of Korea

Correspondence and requests for materials should be addressed to J.S. (email: joonki.suh@kaist.ac.kr)

Data Availability Statements

No primary research results, software or code have been included and no new data were generated or analysed as part of this review.